

Facility to Alleviate Salt Technology Risks (FASTR): Design Report



Kevin Robb
Seth Baird
Jordan Massengale
Ethan Kappes
Padhraic Mulligan

December 2022

**Approved for public release.
Distribution is unlimited.**



DOCUMENT AVAILABILITY

Reports produced after January 1, 1996, are generally available free via OSTI.GOV.

Website www.osti.gov

Reports produced before January 1, 1996, may be purchased by members of the public from the following source:

National Technical Information Service
5285 Port Royal Road
Springfield, VA 22161
Telephone 703-605-6000 (1-800-553-6847)
TDD 703-487-4639
Fax 703-605-6900
E-mail info@ntis.gov
Website <http://classic.ntis.gov/>

Reports are available to DOE employees, DOE contractors, Energy Technology Data Exchange representatives, and International Nuclear Information System representatives from the following source:

Office of Scientific and Technical Information
PO Box 62
Oak Ridge, TN 37831
Telephone 865-576-8401
Fax 865-576-5728
E-mail reports@osti.gov
Website <https://www.osti.gov/>

This report was prepared as an account of work sponsored by an agency of the United States Government. Neither the United States Government nor any agency thereof, nor any of their employees, makes any warranty, express or implied, or assumes any legal liability or responsibility for the accuracy, completeness, or usefulness of any information, apparatus, product, or process disclosed, or represents that its use would not infringe privately owned rights. Reference herein to any specific commercial product, process, or service by trade name, trademark, manufacturer, or otherwise, does not necessarily constitute or imply its endorsement, recommendation, or favoring by the United States Government or any agency thereof. The views and opinions of authors expressed herein do not necessarily state or reflect those of the United States Government or any agency thereof.

Nuclear Energy and Fuel Cycle Division

**FACILITY TO ALLEVIATE SALT TECHNOLOGY RISKS (FASTR):
DESIGN REPORT**

Kevin Robb
Seth Baird
Jordan Massengale
Ethan Kappes
Padhraic Mulligan

December 2022

Prepared by
OAK RIDGE NATIONAL LABORATORY
Oak Ridge, TN 37831
managed by
UT-BATTELLE, LLC
for the
US DEPARTMENT OF ENERGY
under contract DE-AC05-00OR22725

CONTENTS

LIST OF FIGURES	v
LIST OF TABLES	v
ABBREVIATIONS	vii
ACKNOWLEDGMENTS	ix
ABSTRACT.....	1
1. INTRODUCTION	1
2. EXPERIMENTAL DESIGN	3
2.1 FACILITY OVERVIEW & CAPABILITY SUMMARY.....	3
2.2 CHLORIDE SALT	6
2.3 PRIMARY MATERIALS OF CONSTRUCTION.....	6
2.3.1 Corrosion Data Review.....	7
2.3.2 Physical Properties Review.....	10
2.4 SALT PURIFICATION APPROACH AND HARDWARE.....	10
2.4.1 Ventilated Enclosure.....	11
2.4.2 Processing Vessel.....	11
2.4.3 Off-Gas System.....	12
2.5 REDOX CONTROL SCHEME.....	13
2.6 GAS SUPPLY SYSTEM.....	13
2.6.1 Salt Vapor Pressure and Clogging	14
2.7 STORAGE TANK	14
2.8 PUMP, PUMP TANK, AND STAND.....	15
2.9 MAIN HEATER	17
2.10 HEAT EXCHANGER	20
2.11 MAIN PIPING AND TEST PORTS	22
2.12 CORROSION SPECIMENS.....	23
2.13 INSTRUMENTATION	23
2.13.1 Temperature	23
2.13.2 Hazardous Gas Sensors.....	23
2.13.3 Salt Flow Rate.....	23
2.13.4 Salt Chemistry.....	24
2.13.5 Salt Level	24
2.13.6 Gas Pressure and Salt Level Control.....	24
2.14 CONTROL SYSTEM AND TRACE HEATING SUMMARY	25
3. LOOP OPERATING MODES AND CAMPAIGNS	28
3.1 PREDICTED THERMAL-HYDRAULIC OPERATING ENVELOPE AND CONDITIONS	28
3.2 PLANNED TEST CAMPAIGNS.....	30
3.3 POTENTIAL TEST CAMPAIGNS.....	32
3.3.1 Salt-to-sCO ₂ Heat Exchangers.....	32
3.3.2 Salt Valves	32
3.3.3 Instrumentation	32
3.3.4 Off-Gas and Vapor Pressure Effects.....	32
3.3.5 Purification Processes and Online Redox Control	33
3.3.6 Digital Model Validation Testbed.....	33
3.3.7 Handling, Operations and Maintenance.....	33
4. CONCLUDING REMARKS.....	34
5. REFERENCES	35
APPENDIX A. FACILITY INDIVIDUAL SHAKEDOWN CONFIGURATION.....	A-1

APPENDIX B. MAIN HEATER FINITE ELEMENT ANALYSIS B-1
APPENDIX C. PUMP SUMP TANK ANALYSIS..... C-1

LIST OF FIGURES

Figure 1. FASTR layout with red arrows indicating flow direction.	3
Figure 2. FASTR flow loop picture.	4
Figure 3. Enclosure (pictured before heat exchanger installation).	11
Figure 4. Purification processing vessel, scrubber, and storage tank.	12
Figure 5. Storage tank.	14
Figure 6. Pump mounted to pump tank.	16
Figure 7. Pump tank return flow distributor.	17
Figure 8. Main heater: (a) heater plate, (b) insulated assembly illustration, and (c) installed assembly.	19
Figure 9. IR lamp panel assembly.	19
Figure 10. Finned tubing.	20
Figure 11. Heat exchanger: (a) core, (b) inner assembly, and (c) housing assembly.	21
Figure 12. Insulated and installed heat exchanger assembly.	21
Figure 13. Example predicted heat exchanger characteristics (725°C inlet).	22
Figure 14. Corrosion specimen assemblies.	23
Figure 15. Piping and instrumentation diagram.	26
Figure 16. Predicted pressure drop vs. mass flowrate.	29
Figure 17. Maximum heater power at various maximum salt temperatures based on heat exchanger limits.	29
Figure 18. Salt ΔT based on flowrate and main heater power.	30

LIST OF TABLES

Table 1. FASTR requirements and capabilities	5
Table 2. FASTR instrumentation suite	6
Table 3. Composition (wt %) of Hastelloy C-276 and Inconel 600.	7
Table 4. ORNL thermal convection loop testing condition summary	9
Table 5. Purification tank flange nozzles.	12
Table 6. Storage tank flange nozzles	15
Table 7. Pump tank upper plate nozzles	16
Table 8. Gas mass flow controller and pressure transducer sizes	24
Table 9. Pressure relief locations and setpoints	25
Table 10. Heater summary	27
Table 11. Initial test plan.	31

ABBREVIATIONS

AC	alternating current
AlN	aluminum nitride
ANL	Argonne National Laboratory
ASME	American Society of Mechanical Engineers
BPVC	Boiler and Pressure Vessel Code
CFD	computational fluid dynamics
CFM	cubic feet per minute
CSP	concentrated solar power
DC	direct current
DOE	US Department of Energy
EERE	Energy Efficiency and Renewable Energy
FASTR	Facility to Alleviate Salt Technology Risks
FEA	finite element analysis
FMEA	failure modes and effects analysis
Gen3	Generation 3
HX	heat exchanger
I&C	instrumentation and controls
ID	inner diameter
IR	infrared
kPa	kiloPascals
kW	kiloWatt
LED	light emitting diode
lpm	liters per minute
LSTL	liquid salt test loop
MFC	mass flow controller
MW/m ²	MegaWatt per meter squared
OD	outer diameter
PCHE	printed circuit heat exchanger
PLC	programmable logic controller
ppb	parts per billion
ppm	parts per million
psid	pounds per square inch differential
psig	pounds per square inch gauge
PTFE	polytetrafluoroethylene
PVDF	polyvinylidene fluoride
RGA	residual gas analyzer
sch	schedule (pipe)
sCO ₂	supercritical carbon dioxide
SETO	Solar Energy Technologies Office
SLPM	standard liters per minute
SS	stainless steel
TCL	thermal convection loop
UHP	ultra-high purity
UTBDC	UT-Battelle Development Corporation
UTS	ultimate tensile strength
VFD	variable frequency drive
YS	yield strength

ACKNOWLEDGMENTS

The material presented here is based upon work supported by the US Department of Energy (DOE) Office of Energy Efficiency and Renewable Energy (EERE) under Solar Energy Technologies Office (SETO) Agreement Number 33875. The development and construction of a test facility requires contributions from many individuals. Notable contributors at Oak Ridge National Laboratory (ORNL) include Ricardo Muse, Kurt Smith, Graydon Yoder, Jr., David Felde, Roger Kisner, Thomas Roberts, and Heath McCartney, as well as the many skilled craft and support resources. Dave Bozich and Jonathan Neuman at UT-Battelle Development Corporation (UTBDC) and Chad Ator at Ivey Mechanical facilitated design and installation of the ventilated enclosure. Nathaniel Hoyt at Argonne National Laboratory led the development and implementation of the electrochemical sensors. Youyang Zhao at the National Renewable Energy Laboratory provided valuable insight into the purification process and procedure.

ABSTRACT

The Facility to Alleviate Salt Technology Risks (FASTR) is a versatile, high-temperature (>600°C) molten chloride salt test facility designed to enable a variety of testing to advance the Generation 3 (Gen 3) concentrated solar power (CSP) molten salt technology. FASTR includes a salt preparation system and a forced flow test loop with a suite of instrumentation. The FASTR loop is capable of operating at 725°C with flow rates of 3–7 kg/s, and it includes heated and cooled sections and swappable components to enable testing of future vendor-supplied hardware. The salt preparation system supplies large batches (e.g., 200 kg) of clean salt for use in the FASTR forced convection loop. This report summarizes the design and capabilities of FASTR in its as-built form as of December 2022.

1. INTRODUCTION

The Facility to Alleviate Salt Technology Risks (FASTR) is a versatile, high-temperature (>600°C) molten chloride salt test facility designed to enable a variety of testing to advance the Generation 3 (Gen 3) concentrated solar power (CSP) molten salt technology.

Current state-of-the-art CSP plants use nitrate/nitrite salts to transport and store heat. However, in practice, nitrate salt systems are limited to operating temperatures of approximately 585°C. The use of chloride salts enables higher operating temperatures than those currently used in the field, resulting in more efficient power cycles. Furthermore, bulk chloride salts are industrially available at reasonably low costs (e.g., 60-430 \$/1000 kg [1]). For these reasons, chloride salts with higher efficiency power cycles are being investigated by the Solar Energy Technologies Office (SETO) of the US Department of Energy (DOE) Office of Energy Efficiency and Renewable Energy (EERE) to enhance the economic competitiveness of CSP [1].

Before a chloride salt-based Gen 3 CSP plant is deployed, several technological challenges and demonstrations must be addressed, including salt sourcing, preparation, and monitoring; component design, supply chain, and reliability; and corrosion control [1]. The number of test facilities available to mature and de-risk the required technology for molten chloride salts is limited. To address this need, SETO sponsored the development, construction, and the initial operation of FASTR at the Oak Ridge National Laboratory.

FASTR includes a salt preparation system and a forced flow test loop with a suite of instrumentation. The FASTR loop is capable of operating at 725°C, with flow rates of 3–7 kg/s. FASTR includes heated and cooled sections and swappable components to enable testing of future vendor-supplied hardware. The salt preparation system supplies large batches (e.g., 200 kg) of clean salt for use in the FASTR forced convection loop. The project includes additional efforts focused on developing and demonstrating innovative electrochemical sensors to monitor the salt and structural materials.

FASTR and its accompanying research data will serve as a foundational capability to advance this promising Gen3 CSP technology. Once built, FASTR will be the largest high-temperature (i.e., >600°C) molten salt test facility operating in the United States. Key facility demonstrations include corrosion monitoring and control, as well as performance demonstrations of major components such as flanges, heat trace, heat exchangers, pumps, and so on. FASTR will de-risk high-temperature molten salt technology and will demonstrate the viability of the Gen3 molten salt pathway.

In parallel to the design, construction, and operation of FASTR, a separate effort led by the National Renewable Energy Laboratory (NREL) prepared a design for a 2 MW pilot-scale chloride salt CSP facility [2, 3]. Separately, the pre-conceptual design for a simplified plant based on a thermocline was

proposed [4]. FASTR serves as an intermediate-scale test facility between smaller bench-scale testing facilities and larger pilot-scale facilities.

The preliminary facility design is described in a report by Robb et al. [5], which details a failure modes and effects analysis (FMEA) that was conducted to inform design choices and reduce the risk of issues during operation. The FMEA results remain relevant but are not reproduced herein. This report summarizes FASTR's as-built design and capabilities: the specifications presented herein supersede the description in the preliminary design report [5]. For completeness, some details in the preliminary design report are reproduced in this report. As of this writing, system shakedown testing has been completed, and efforts are progressing toward pump operation. Some modifications during startup may result in configuration deviations from the design described in this report.

2. EXPERIMENTAL DESIGN

2.1 FACILITY OVERVIEW & CAPABILITY SUMMARY

A schematic of FASTR is provided in Figure 1. The as-built system is shown in Figure 2. The salt preparation is conducted inside a ventilated enclosure. A separate storage tank for the salt is also located in the enclosure. Transfer lines, which are not illustrated in Figure 1, interconnect the processing, storage, and pump vessels. The pump is located outside the enclosure, and it forces salt in a counterclockwise direction around the loop. The main heater supplies the majority of heat to the salt, and an air-cooled heat exchanger removes heat from the loop. Trace heating, insulation, and instrumentation are located throughout the facility. The key technical specifications and capabilities for FASTR are summarized in Table 1. A separate summary of the instrumentation and controls (I&C) capabilities is highlighted in Table 2. The following subsections provide further descriptions of the various major components.

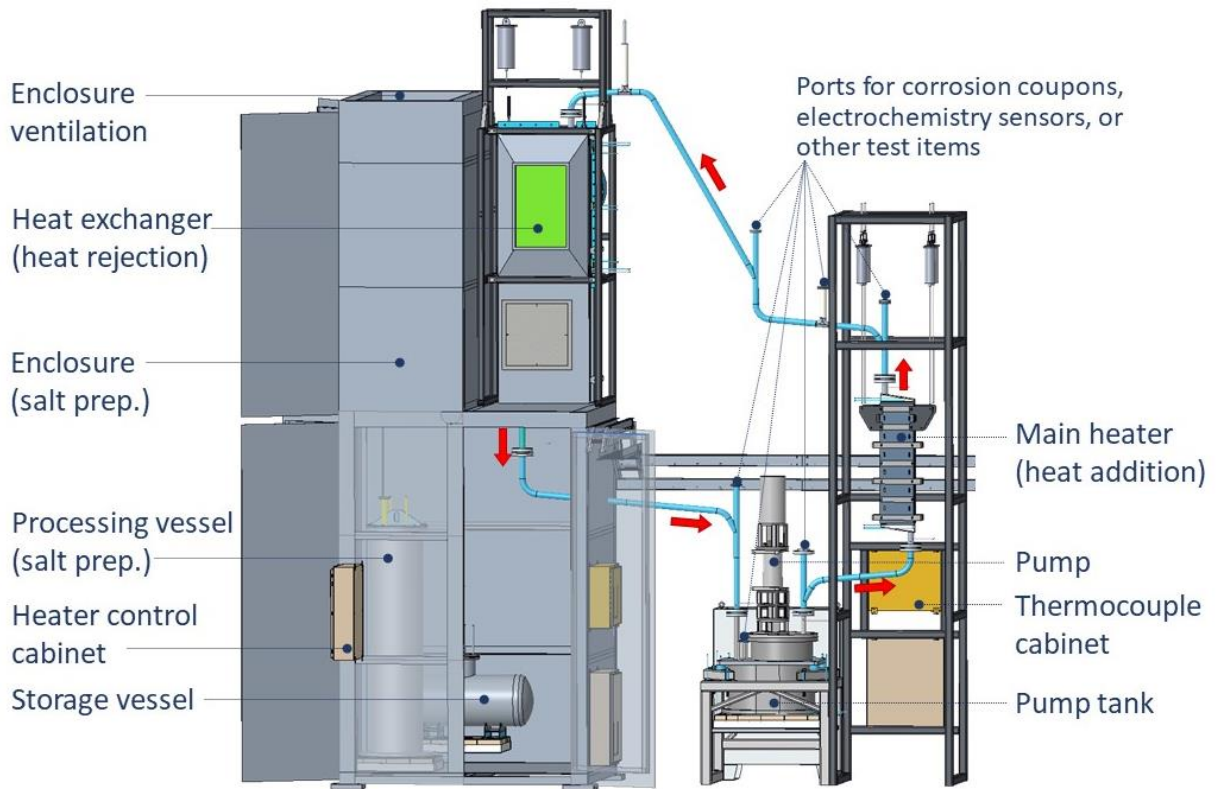


Figure 1. FASTR layout with red arrows indicating flow direction.

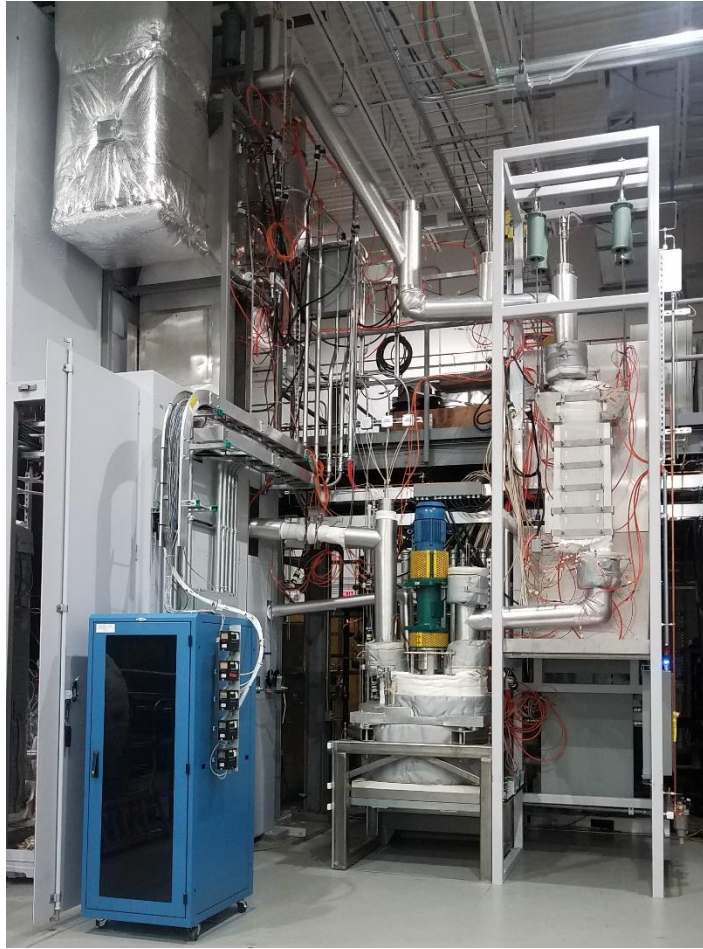


Figure 2. FASTR flow loop picture.

Table 1. FASTR requirements and capabilities

Capability	Detail	Value	Units	Comments	
System design temperature	Hot side	725	°C		
Primary alloys of construction		C-276 600	-		
Primary piping size		2	in.	Schedule 40, seamless	
System design pressure	Salt processing	206	kPa	30 psig	
	Flow loop	145–310	kPa	21–45 psig	
Salt flow rate	Mass flow rate	3–7	kg/s	3–6 kg/s is primary goal	
	Volume flow rate	114–228	lpm	30–70 gpm	
Salt volume/mass	Purification system	≥200	kg	if loaded as powder/granules	
	Salt loop	120	L	200 kg (~120 L, 32 gallon)	
Main heater	Power	Capacity	400	kW _{th}	To the salt
		Current heaters	103	kW _{th}	144 kW _e with assumed 72% efficiency of energy delivered to test section
	Max. heat flux	Design	1,000	kW/m ²	To the salt
		Current heaters	580	kW/m ²	Estimated
	Axial zones	6	qty		
	Reynolds number (salt)	15,000–50,000	-		In channels, based on estimated salt properties
Trace heating	Controlled zones	48	qty		
	Total power	65	kW		
Test ports	Locations	6	qty	3× hot zone, 3× cold zone (e.g., corrosion samples, sensors)	

Table 2. FASTR instrumentation suite

Instrumentation suite	Detail	Qty	Units
Pressure	Gas space	6	Places
Gas mass flow controller	Gas space	12	Places
Salt flow rate	Ultrasonic	1	Places
Salt level	Thermocouple probe	4	Places
Hazardous gas detectors	HCl & Cl ₂	3	Places
	H ₂	2	Places
Humidity	System off-gas	1*	Places
pH	System off-gas	1	Places
Residual gas analyzer (RGA)	System off-gas	1	Places
Temperature: thermocouples	<i>Main heater</i>	48	<i>qty</i>
	<i>Trace heating</i>	89	<i>qty</i>
	<i>Flowmeter</i>	2	<i>qty</i>
	<i>Heat exchanger</i>	21	<i>qty</i>
	<i>Level probes</i>	40	<i>qty</i>
	Total	200	qty
Salt redox potential & specie concentrations	Multielectrode array voltammetry sensor with dynamic reference	4	Places

*Sensor failed

2.2 CHLORIDE SALT

Chloride salts are being considered for Gen3 CSP based on their attractive economics, their ability to operate at high temperatures while at low pressure, and their heat storage capability. A mixture of NaCl, KCl and MgCl₂ salts was chosen based on their attractive economics and their ability to form a low melting point mixture.

The salt is a mixture of two industrially available chloride salt mixtures. An anhydrous carnallite (nominal wt% of 9–18 NaCl, 36–43 KCl, and 43–52 MgCl₂ with traces of MgO, C, H₂O, and SO₄), will be used as the base salt. To increase the NaCl concentration of the salt to yield a lower melting point mixture, a halite salt will be added (nominal wt% of 92.5 NaCl, 6 KCl, and 1.4 CaSO₄•2H₂O with traces of LiCl and MgCl₂). After purification, the wt% of the final salt mixture was measured to be 18.6 NaCl, 38.1 KCl, 42.9 MgCl₂, and 0.4 CaCl₂ with a melting point of approximately 400°C.

2.3 PRIMARY MATERIALS OF CONSTRUCTION

The primary alloys of construction were selected based on high-temperature capability, anticipated corrosion resistance, and commercial availability. To accommodate the project timeline, alloys of construction were selected before rigorous corrosion test data were available. Before project startup, it was known that molten chloride salts preferentially attack chromium, but many high-temperature alloys contain substantial chromium concentrations to inhibit oxidation in air and water. Although alloys C-276 and 600 have chromium in the 14–17 wt% range, these concentrations are lower than many other high temperature alloys (e.g., 230, 304H, 310, 617, 625, 740H, and 800H).

Ultimately, alloys C-276 and 600 (Table 3) were selected as the primary materials for FASTR [6, 7]. All salt-wetted surfaces are C-276 except for the main heater (Section 2.9) and level probes (Section 2.13.5),

which are constructed of alloy 600. Alloy C-276 is used industrially for its exceptional resistance to stress corrosion cracking and to halides (i.e., Cl⁻ and F⁻). Both alloy 600 and C-276 are used throughout the chemical industry, so they are reasonably available and have 50+ year track records. Sections 2.3.1 and 2.3.2 provide additional insights as to the selection of these materials with respect to their corrosion resistance and other physical properties.

Table 3. Composition (wt %) of Hastelloy C-276 and Inconel 600

Alloy	Ni	Cr	W	Mo	Fe	Co	Mn	Si	V	Cu	C	S
C-276 [6]	57 Bal	16	4	16	5	2.5 Max	1 Max	0.08	0.35 Max	0.5 Max	0.01 Max	
600 [7]	72 Min	14-17			6-10		1 Max	0.50 Max		0.50 Max	0.15 Max	0.015 Max

2.3.1 Corrosion Data Review

Although an exhaustive review of corrosion testing is not the focus of this report, the literature discussed in the following sections provides confidence and continues to support the materials selected for the FASTR facility with respect to corrosion resistance.

2.3.1.1 Static and Isothermal Liquid Corrosion Tests

Most corrosion test data are from static isothermal tests. These types of tests are useful for screening and comparing alloys under the same conditions. Because of the differences in salt preparation, sample-to-salt area/volume ratio, container material, and test time and temperature, the following brief review does not compare results between different studies.

Limited studies have been conducted to determine the corrosion resistance of alloy C-276 and 600 to that of molten ternary NaCl-KCl-MgCl₂ salt:

- Sun [8] evaluated stainless steel (SS) 316 and seven Ni-based alloys at 700°C for 100 h. With respect to Cr depletion depth, C-276 was the top performer in corrosion resistance. This was attributed to its high molybdenum content.
- Sun [9] studied the corrosion rate of Hastelloy N, C-276, C22, and Haynes 230 for 400 h of exposure at 600, 700, and 800°C. In general, the chromium depletion depth of alloys N, C-276, and C22 were similar, with alloy N performing the best, and C22 performing slightly worse. The chromium depletion of alloy 230 was more severe than the other three nickel alloys.
- Ding [13] compared the corrosion rates of C-276, Inconel 800H, and 310SS in ternary salt at 700°C for 500 hours with and without the addition of 1 wt% Mg to the salt. The C-276 material performed substantially better than 800H and 310SS with and without the addition of Mg. The Mg addition substantially reduced corrosion rates for all alloys.
- Pint [25] investigated the impact of a range of parameters on the corrosion in capsule tests. In one series of tests (800°C for 100 h), they demonstrated a nearly linear increase in the corrosion rate, with alloy chromium content of alloys 244, 600, and 230. A series of tests exposed alloy 600 and C-276 inside alloy 600 capsules for 1,000 h at temperatures of 600–800°C. Although the mass loss was higher for the C-276 specimens, the attack was more uniform, and the depth of attack was lower than

the alloy 600 specimens. Both alloys experienced relatively low corrosion rates. They also demonstrated that the inclusion of metallic Mg reduced the corrosion rate.

- D'Souza [27, 29] compared the corrosion of alloys 718, 709, 316L, 230, and C-276 exposed in the ternary salt at 800°C for 100 h. On a mass loss basis, C-276 performed the best.
- Keiser [30] studied the corrosion of five metallic alloys and five nonmetallic materials (e.g., ceramics) at 750°C for 500 h. On a mass loss basis of the metallic alloys, C-276 and 600 performed similarly and better than alloys 230, 244, and Tribaloy 900. C-276 also experienced the smallest depth of attack noticed in cross-sectional light micrographs.

Additional supporting corrosion results for non- NaCl-KCl-MgCl₂ salts can be found in the literature. Although these results are not in the salt of interest, the following results further inform material selection. Vignarooban [10] compared the corrosion rates of C-276, C-22, and Hastelloy N in NaCl-KCl-ZnCl₂ salt. At 500°C, C-276 was the top performer. Mohammad [14] investigated Haynes 230 and C-276 in molten MgCl₂-KCl at 800°C for 336 and 384 h. The C-276 alloy experienced less corrosion than the Haynes 230. Pillai [12] compared the corrosion of alloy C-276 and 600 in MgCl₂-KCl at 700°C for 1,000 h. Both alloys experienced similar chromium depletion depth.

2.3.1.2 Static and Isothermal Vapor Corrosion Tests

Corrosion in the vapor space above molten NaCl-KCl-MgCl₂ salts has been studied less extensively than in the liquid phase. Two studies were identified noting that corrosion in the space can be appreciable. In addition to salt species, HCl can exist in the gas space. Hot HCl, especially in the presence of moisture, is known to be corrosive.

- D'Souza [27, 28] compared the corrosion of alloy 230 after 100 h at 800°C in salts with different preparation procedures. One test case included coupons only in the vapor space above nonpurified salt. That test did not include immersed coupons, so a direct comparison is not available. However, the coupons exposed to the vapor space experienced mass losses comparable to the immersed coupons in other tests.
- Liu [30, 32] studied the vapor and liquid corrosion of NaCl-KCl-MgCl₂ salt at 700°C on 316SS and a Ni-Mo-Cr alloy. The experiments were conducted in alumina crucibles sealed in argon. The Ni-Mo-Cr alloy (wt%: 70.56 Ni, 17.34 Mo, 7.01 Cr, 3.92 Fe, and minor elements) is similar to that of Hastelloy N. After 100 hours, the iron and chromium depletion depth of the Ni-Mo-Cr alloy in the vapor space was approximately 240% greater than that of the samples immersed in the liquid salt [30]. Comparing results from both studies, the iron and chromium depletion depths in the 316SS alloy (20 μm) were approximately 70% greater than the Ni-Mo-Cr alloy (12 μm).

2.3.1.3 Flowing and Non-Isothermal Corrosion Tests

Beyond static capsule corrosion tests, more prototypic corrosion rates have been determined through tests with flowing salt and a temperature gradient. The solubility of various corrosion products such as CrCl₃ varies with temperature. Temperature gradients, as seen in the end application, are known to influence the corrosion and deposition process. The few such corrosion tests that have been conducted to date are discussed herein. However, the results provide confidence and generally support the choice of using alloys 600 and C-276 for FASTR.

Thermal convection loops (TCLs), also termed *harp loops* based on their appearance, are formed by piping in the shape of a parallelogram. One vertical leg is heated while the other is cooled. The density difference of the salt between the hot and cold legs induces a natural convective flow around the loop.

Historically, Oak Ridge National Laboratory (ORNL) has operated hundreds of these loops to test molten salt compatibility, as well as molten metals and other fluids. More recently, SETO sponsored the operation of three TCLs at ORNL [25]. All loops were constructed of Inconel 600 with 1-inch outer diameter (OD) tubing, all used industrially sourced NaCl-KCl-MgCl₂ salt, and all had 0.04–0.05 wt% of metallic Mg added. Table 4 summarizes the range of test conditions. Overall, the testing demonstrated that low corrosion rates could be achieved. The report [25] documents the details and findings of the extensive study.

Table 4. ORNL thermal convection loop testing condition summary

Parameter	Loop #1	Loop #2	Loop #3
Operating time (h)	1,000	110	1000
Number of specimens × alloy	40 × 600	20 × 600, 20 × C-276	20 × 600, 20 × C-276
Sample temperature range (°C)	580–700	580–750	565–700
Salt mass (kg)	2.3	2.5	5
Comments		Re-used Loop #1 Electrical failure halted operation	Possible air ingress during test

Like the thermal convection loops operated by ORNL, smaller microloops were developed and operated by TerraPower LLC [33]. Because of the size of the loops and the 0.25 in. OD of the tubing, the tubing itself is used as corrosion specimens. A recent paper summarized an extensive study of 49 loops totaling approximately 9 years of flow time. Of the nine alloys tested, only alloy 600, alloy C-276, and alloy N had corrosion rates less than 100 μm/y.

Three microloops constructed of alloy C-276 were operated with NaCl-MgCl₂ eutectic, with a maximum hot leg temperature of 620°C and a minimum cold leg temperature ranging from 496–513°C (i.e., approximately 107–124°C temperature gradient) [33]. Two of the loops operated for a year or longer at 8,747 and 10,081 h. The formation of deep chasms (e.g., 180 μm) was a notable difference between these otherwise similar loops. The two loops were found to have differences in their microstructures, and further investigation suggested that the chasms were caused by precipitates that were introduced during the tube extrusion process.

Results for eight alloy 600 microloops are presented in the paper by Kelleher et al. [33], with two microloops using NaCl-KCl-MgCl₂ and the remainder using NaCl-MgCl₂. The corrosion depth and microstructure results were similar for the two salts when compared under similar operating conditions. The results also suggest that alloy mass loss caused by corrosion was less for the salts that were contacted with Mg during the purification process compared to salts that were not.

Test experience with alloy 316 microloops was not favorable and resulted in premature test termination. For test results using alloys N, 617, 625, 800H, and 200/201, the reader is referred to the paper by Kelleher et al. [33]. Finally, most of the test results presented had a maximum hot leg temperature of 620°C and a cold leg minimum temperature of approximately 500°C, both lower than the ORNL TCL test results, most of the static capsule test results, the planned FASTR test campaign results, and the SunShot program goals. However, the presented test campaign is among the most thorough exploration of molten chloride salt corrosion under a more prototypic temperature gradient to date.

2.3.2 Physical Properties Review

Alloy C-276 is approved for use by the American Society of Mechanical Engineers (ASME) Boiler and Pressure Vessel Code (BPVC) Section VIII for pressure vessels, and it approved for use in ASME B31.3 for process piping up to 1,250°F (676°C). The codes note that the allowed stresses are time dependent, and they provide values up to 700°C to aid design. The allowed stresses for alloy C-276 for temperatures >600°C are approximately 5 times greater than those for alloy 600.

FASTR has a high-temperature goal of 725°C. To support this, a literature review of C-276 high temperature (>675°C) properties was initiated, focusing on high-temperature creep properties. A preliminary review indicated that C-276 creep properties at 750°C appear to align with the values for Hastelloy S and alloy 600. Because the data from open literature data were limited, a major metal manufacturer was contacted and provided creep data for temperatures up to 982°C. This literature review and analysis is summarized in a paper by Ren and Robb [15]. Ultimately, allowed stress values of 39.3 MPa (5.7 ksi) at 725°C (1,337°F) and 45.2 MPa (6.5 ksi) at 704°C (1,300°F) were chosen for design. To monitor the material's long-term performance, specimens will be included for periodic inspection.

The impact of the salt on the material properties has been investigated by Xu et al. [11], Pint et al. [25], and D'Souza [27].

- While results are limited, the work by Xu et al. [11] showed that C-276 and Haynes 230 have comparable reductions in strength at high temperatures. This reduction was independent of the high-temperature environment with two different chloride salts and argon. This suggests that the impact on strength was primarily caused thermal effects instead of salt exposure.
- In the work by Pint et al. [25], tensile specimens of C-276 and 600 were exposed in the ternary salt of interest in the thermal convection loops. For the C-276 samples exposed for 1,000 h in the salt, the ultimate tensile strength (UTS) and yield strength (YS) both decreased with increasing exposure temperature as compared to the unexposed material. In comparison to the exposed alloy 600 samples, the C-276 samples in the cold leg had higher UTSs, and the samples in the hot leg had similar UTSs. The YSs of the C-276 samples were higher than those of the alloy 600 samples for all exposure temperatures. The elongation of the C-276 samples decreased from 85–90% for the unexposed samples to 40–60% for the exposed samples, with the largest reduction occurring at the higher exposure temperatures. There was a marked decline between the samples exposed at and below 670°C compared to the samples exposed to 680°C and higher. Unfortunately, the study did not include samples for comparison that had been heated but not exposed to salt.
- D'Souza [27] measured the hardness and YS of C-276 samples exposed to the ternary salt of interest at 800°C for 100 hours. Compared to nonexposed specimens, the specimens exposed to high-temperature salt increased in both hardness and YS.

2.4 SALT PURIFICATION APPROACH AND HARDWARE

Anhydrous chloride salts, particularly $MgCl_2$, readily absorb moisture. The presence of moisture and hydroxides in the salt is known to increase corrosion. The complex hydroxides of $MgCl_2$ (e.g., $MgCl_2 \cdot 6H_2O$, $MgCl_2 \cdot 4H_2O$, and $MgCl_2 \cdot 2H_2O$) are reduced at elevated temperatures, thus liberating H_2O and HCl . However, $MgCl_2 \cdot H_2O$ can undergo partial hydrolysis, forming $MgOHCl$. $MgOHCl$ is difficult to remove, requiring a more rigor than vacuum heating the salt.

A process was developed using metallic Mg to reduce $MgCl_2OH_x$ and to set a low redox potential. The following sections summarize the infrastructure for the process, including the ventilated enclosure, the

processing vessel, and the effluent scrubber. Further details on the process and hardware, as well as the system's first operation are documented in the report by Robb et al. [43].

2.4.1 Ventilated Enclosure

The purification process for the chloride salt was undetermined at the project's onset. Therefore, a ventilated enclosure capable of confining potential hazardous gases was included. The enclosure has an 8 × 8 ft (2.44 × 2.44 m) floor area. Half of the enclosure is 22 ft (6.7 m) tall, and the other half is 12 ft (3.66 m) tall, as shown in Figure 3. The taller section includes a chain hoist that is used to lift the processing vessel, the vessel liner, the lid, and the transfer lines. The heat exchanger described in Section 2.10 sits atop the shorter 12-foot section. The enclosure is ventilated with outside air, with the supply entering towards the bottom, and the return ductwork is located at the top. The return houses a blower with a capacity of 3,000 cubic feet per minute (CFM) and is controlled via a variable frequency drive (VFD).



Figure 3. Enclosure (pictured before heat exchanger installation).

2.4.2 Processing Vessel

The processing vessel shown on the right of Figure 4 is made of C-276 and includes an inner C-276 liner. The vessel has an internal height of 86.7 inches and diameter of 19.5 inches. It was designed to accommodate a pressure of 206.8 kPa (30 psig) at 700°C, and it was sized to hold a batch of powdered

salt ranging up to 400 kg, which would yield approximately 240 liters of liquid salt. The capacity depends on the packing fraction of the raw material. The lid includes four nozzles, as described in Table 5. A heater blanket surrounds the tank with three vertical heater zones, and the vessel sits atop a custom designed heater plate (see Section 2.14). A firebrick tray is located beneath the heater plate.

Table 5. Purification tank flange nozzles

Nozzle inner diameter (ID) (in.)	Baseline purpose
2.067	Electrochemical sensor
0.620	Sweep gas
0.620	Bubbler tube
0.620	Gas outlet



Figure 4. Purification processing vessel, scrubber, and storage tank.

2.4.3 Off-Gas System

The effluent from the processing vessel is vented through a scrubber system designed to capture H₂O and HCl. The system consists of a vacuum break tank and a series of three scrubber tanks. All tanks and lines

are made of chemical-resistant plastics such as polytetrafluoroethylene (PTFE). The vacuum break prevents water in the scrubbers from backflowing into the processing vessel if there is a loss of pressure control in the processing vessel caused by power failure accompanied by vessel cooldown, for example. The vacuum break and three scrubber tanks are partially filled with deionized water. The effluent is passed through the gas space of the vacuum break and through bubbler tubes in the three scrubbers. After the effluent has gone through the final scrubber, it is vented towards the top of the ventilated enclosure.

Two hazardous gas sensors survey the gas space inside the enclosure. These detectors have been set for hydrogen chloride and hydrogen, but different species can be selected for detection. The sensors are connected to the programmable logic controller (PLC). If hazardous conditions are detected, then the operations are altered, and argon bubbling into the salt is stopped.

The off-gas system includes a suite of instrumentation to monitor the process. Between the processing vessel and the scrubber, a humidity sensor is located in-line. The sensor (Vaisala HMT334) has a range of 0–100 % relative humidity and can operate at temperatures up to 180°C. This sensor failed during salt purification because of the corrosive off-gas [43]. A residual gas analyzer (Stanford Research Systems UGA100) uses a mass spectrometer to analyze a small sample stream of gas taken from the main off-gas line. The online sampling and pH measurement system shown in the central area of Figure 4 is integrated into the vacuum break and the first scrubber tanks of the scrubber system. A small diaphragm pump made of chemically resistant materials (e.g., PTFE, polyvinylidene fluoride [PVDF]) takes suction from the vacuum break tank and forces the fluid through a pH sensor (Valmet 4338) before it returns to the tank.

2.5 REDOX CONTROL SCHEME

During loop operations, air, moisture, and other impurities could inadvertently be introduced into the system. The air and moisture would interact with the salt, changing its redox potential and increasing its corrosivity. Metallic magnesium has been shown to be effective at purifying relevant chloride salts. This experience is explained by basic salt chemistry as illustrated by an Ellingham diagram. MgCl_2 has the highest redox potential of the salt constituents (i.e., MgCl_2 , NaCl , KCl), and it has a redox potential below that of potential corrosion products of the metallic system (e.g., chlorides of Cr, Fe, Ni, and Mo). Having Mg available in the system fixes the redox potential below that of the structural alloy corrosion products, inhibiting their formation while also maintaining a high enough redox potential to prevent reduction of the other salt constituents. For a more thorough discussion, the reader is referred to references on molten salt chemistry such as Ambrosek's dissertation [21]. Based on the previous purification experiences using Mg and the basic salt chemistry of the system of interest, it follows that adding Mg to the FASTR system will assist in maintaining the salt purity and ensuring a sufficiently low redox potential to inhibit corrosion of the system hardware. Indeed, adding Mg to chloride salt has been shown to reduce corrosion during static corrosion tests [13, 23, 24] and small natural convection driven loops [25], as described in Section 2.3.1. For these reasons, Mg contact will be incorporated into the FASTR system to inhibit corrosion. The plan is to use commercially sourced Mg rods of 99.9% assay purity with a diameter of 4.8 mm and a length of 200 mm (approximately 6.25 g). One end of the Mg rods is threaded and attached to a stainless-steel rod which will be inserted through a port in the pump tank using a ball valve arrangement.

2.6 GAS SUPPLY SYSTEM

Argon is used as a cover gas and to pneumatically move salts from one vessel to another. The gas supply system includes a source of argon, a gas supply panel, a gas purifier, and downstream mass flow controllers. Ultra-high purity (UHP) argon is supplied either via a 16-pack of large (i.e., 300 ft³) high-pressure bottles or from a large cryogenic liquid argon tank (e.g., 270 L). UHP has a specification of 99.999% purity with a maximum of 1 ppm O₂, 1 ppm H₂O, and traces of CO, CO₂ and N₂. The supply panel includes a pressure regulator with the pressure relief set to 90 psig, and isolation valves. A bank of

six parallel combined oxygen and moisture molecular sieve traps is used to remove traces of O₂, H₂O, CO₂, and CO in the UHP gas or that is inadvertently introduced at the gas supply. Each trap has a capacity of 3.2 g of O₂ and 13.6 g of H₂O (at 100% capacity). The purifier was sized to accommodate at least 60 standard liters per minute (SLPM) of flow and can purify at least 420 × 300 ft³ bottles of UHP argon to impurity concentrations of ppb. Once the argon leaves the gas purifier, it is piped to mass flow controllers (MFCs) to perform various functions (see Section 2.13.6).

2.6.1 Salt Vapor Pressure and Clogging

It has been established that molten salts with high vapor pressures can impact off-gas systems. A vapor pressure on the order of 1 mm Hg or lower represents a target to reduce the complexity of off-gas systems [40].

Empirical evidence obtained during early testing with representative ternary chloride salts suggests that the salt has appreciable vapor pressure (i.e., substantial mass loss of molten salt at high temperature under inert conditions). This empirical evidence continues to be observed in other testing. During construction of FASTR, another team measured the vapor pressure of the salt [41]. Their tests indicated vapor pressures on the order of 35 mbar (26 mm Hg) at 725°C. However, it is unclear how the vapor pressure was measured because the system included a condenser to intentionally remove salt vapors from the gas space. Although it is not discussed in detail in the results, the instrumentation uncertainty is also substantial compared to pressures measured.

Four mitigation strategies will be employed to mitigate the impact of condensing vapors.

- Ports will be maintained at a lower temperature (e.g., 500°C) to decrease the vapor pressure and to encourage condensation and return of vapors before exiting the ports.
- The gas lines include tees or crosses to facilitate boring of out-gas lines either as a preventative measure or once they become clogged.
- Most venting locations include redundant off-gas lines.
- Filters were placed upstream of the MFCs on the vent lines to inhibit fouling of the instruments.

Operation experience from FASTR will provide practical insight as to the effects of the vapor pressure, whether gas lines clog, and the efficacy of associated prevention and remediation efforts.

2.7 STORAGE TANK

The storage tank (Figure 5) stores the salt when not in use, and it is designed to accommodate salt freeze/thaw cycles. It is made of C-276 and has a total volume of approximately 240 L. The vessel is a horizontal cylinder with semi-spherical heads designed to accommodate a pressure of 206.8 kPa (30 psig) at 700°C. The tank includes several nozzles, as summarized in Table 6. A heater blanket surrounds the tank that includes three heater zones positioned vertically and 4 inches of high-temperature insulation. The storage tank is placed on top of a firebrick tray. A scale under the firebrick tray is used to monitor and record changes in salt mass.



Figure 5. Storage tank.

Table 6. Storage tank flange nozzles

Nozzle ID (in.)	Baseline purpose
0.680	Salt transfer
0.555	Salt transfer
0.430	Gas inlet and outlet
0.430	Spare
0.180	Level probe
0.180	Level probe
0.180	Spare / electronic chemical sensor
0.180	Spare / electronic chemical sensor

2.8 PUMP, PUMP TANK, AND STAND

A custom high-temperature molten salt pump is used to circulate the salt in the loop. A cantilevered centrifugal-type pump was selected. This type of pump does not have seals or bearings located in the salt. The salt pump was competitively sourced, and the wetted materials are constructed of C-276. The shaft seal uses a noncontacting gas-lubricated model for high temperatures (John Crane 2874NE). This type of seal is similar to that demonstrated on the liquid salt test loop (LSTL) [36]. During operation, the seal is formed by application of a thin layer of argon.

The pump produces up to 70 gpm at 29 ft of head, with a maximum temperature rating of 1,337°F (725°C). A VFD connected to the PLC (see Section 2.14) controls the speed of the motor and therefore the salt flow rate. The low-speed range of the pump depends on seal performance and is anticipated to be 30 gpm.



Figure 6. Pump mounted to pump tank.

The pump is inserted into the ORNL-designed pump tank. To limit the salt volume, the tank was designed with an obround shape, which is two semicircles joined together with flat regions in between. A separate mounting flange for the pump is located above the upper plate of the tank. The pump can be removed while the tank remains in place. A stand supports the upper plate of the tank and is designed to accommodate the tank's lateral and vertical thermal expansion. Originally, the upper plate was designed to be a flange to enable inspection of the volute and impeller of the pump. However, this feature was eliminated to reduce tank cost. The salt return line penetrates through the upper plate. Several other nozzles also penetrate the top of the tank, as summarized in Table 7.

Table 7. Pump tank upper plate nozzles

Location	Nozzle ID (in.)	Baseline purpose
Upper plate	2.067	Large test port - sensor
	0.902	Spare
	0.902	Salt fill/drain
	0.430	Level probe
	0.430	Level probe
Pump mounting flange	0.430	Cover gas inlet/vent
	0.430	Spare

Given the nontraditional design, a finite element stress analysis was conducted using ANSYS (see Appendix B). Based on the analysis, the tank is capable of 21.5 psig pressure at 704°C (1,300°F).

To reduce agitation of the salt free-surface and entrainment of gases into the salt, the loop return line discharges into a flow distributor, Figure 7. The flow distributor is made of two stacked C-276 plates at the bottom of the tank that are tack welded into place to prevent movement. A small gap between the flow distributor and tank wall facilitates distributed discharge of the salt into the tank. Computational fluid dynamics (CFD) was used to optimize the flow distributor design and to confirm that no gas entrainment is predicted [5].



Figure 7. Pump tank return flow distributor.

2.9 MAIN HEATER

FASTR includes heated and cooled sections so that a temperature difference can be formed across the loop as required for prototypic corrosion studies.

The design goal for the heater is to provide salt at up to 725°C at the outlet and to have a peak attainable heat flux to the salt of 1 MW/m² and an overall power of 300 kW. Various options for the main heater were explored, including induction, direct joule heating of the piping, natural gas, quartz near infrared (IR) lamps, xenon lamps, high-powered light emitting diodes, and traditional resistance-based heaters. The need to achieve a high heat flux at high temperatures, combined with overall system cost limitations, drove the down-selection process.

A flat plate geometry was chosen for the main heater shown in Figure 8A. It is composed of a single 0.75-inch thick Inconel 600 plate measuring 46.25 inches long and 13 inches wide. Fourteen holes 0.313 inches in diameter were gun drilled at a 0.785-inch pitch through the length of the plate. These holes serve as vertical salt flow channels. The dimensions were determined through an optimization study using finite element thermal analysis to achieve uniform temperature distributions in the salt channel, maximum heat flux, and minimum peak temperature while conforming to real-world machinable dimensions. Inconel 600 was selected as the heater plate material because of its slightly higher thermal conductivity and its coefficient of thermal expansion that is similar to C-276. The higher thermal conductivity reduces the temperature distribution in the heater plate and reduces the plate's maximum temperature. The front and rear faces of the plate contain twelve 0.063-inch channels for thermocouple placement. Holes on either

edge of the plate are used to mount the plate and to secure heating elements and insulation to the plate's front and rear faces (Figure 8). Plate temperatures are regulated using six axial heater zones that are independently controlled. Salt enters the main heater through the bottom plenum and exits through the top plenum. The main heater assembly shown in Figure 8B is suspended using spring hangars attached to a tubular frame.

The initial plan was for the system to use aluminum nitride (AlN) heaters placed onto a flat rectangular main heater plate. Twelve flat AlN heaters (2 units wide \times 6 units high) were designed to be placed against each side of the main heater plate. A spring-loaded stack up of insulation would compress the heaters against the plate while also accommodating thermal expansion. Testing of prototype heating elements using a direct current (DC) power supply identified changes to improve the design. Testing of the revised heating elements with the alternating current (AC) power controllers installed resulted in early failures at relatively low powers and low temperatures compared to the performance targets. The cause was suspected to be localized heating in the elements stemming from potential high frequencies that could be generated in the AC power controllers. The cause was not fully explored before the decision was made to switch to an alternate heating method.

Two heating alternatives were explored: cartridge heaters and IR lamps. The cartridge heaters could not meet the high heat fluxes desired for the testing [42]. Therefore, IR lamps were pursued. Eight IR lamp units (model Hi-TempIR 5203-10, 18 kW_e each) were purchased. With an assumed 72% efficiency (heat deposited onto target), the eight lamps can provide approximately 103 kW_{th} to the heater plate. The lamps are positioned over the center of the bottom four heating zones. The lamp modules are positioned 4 in. (102 mm) away from the plate to facilitate smoothing of the applied heat flux over the plate surface. Stainless steel reflectors polished with 2000 grit sandpaper occupy the space between the IR lamps. An assembly of four IR lamp units and three reflectors is shown in Figure 9. For future expansion, the heating plate and heater controller are sized to accommodate 24 lamps (i.e., 310 kW_{th} delivered to plate). The lamps require air and chilled water cooling. Because these utilities could not be fully installed prior to operation, heater tape was applied to the main heater surface and used for initial operations.

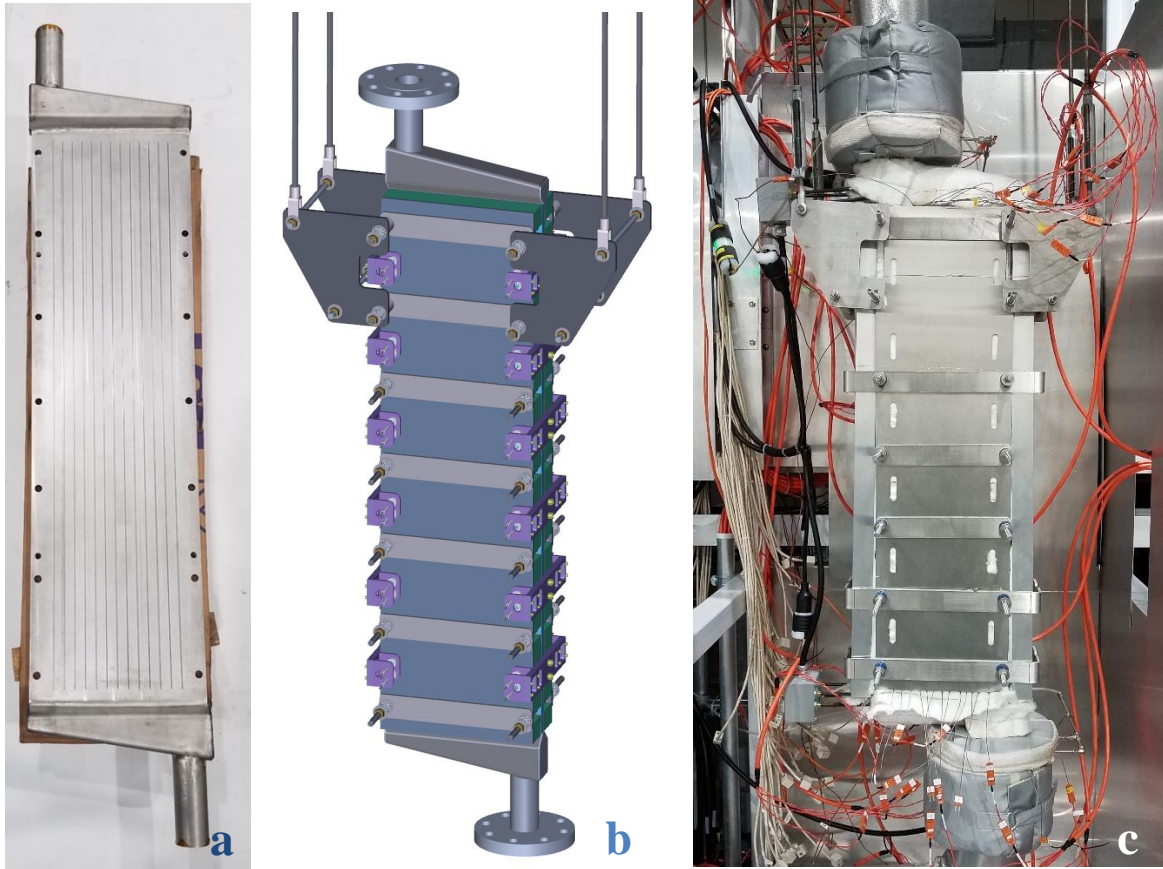


Figure 9. IR lamp panel assembly.

2.10 HEAT EXCHANGER

An air-cooled heat exchanger was chosen to reject heat from the loop. ORNL's LSTL uses a finned tube air-cooled heat exchanger to reject heat [35, 36]. This existing design and ORNL's relevant experience were leveraged to design the heat exchanger for FASTR.

The following design constraints were applied when sizing the heat exchanger. The heat exchanger is to reject up to 350 kW_{th}. The predicted surface temperature was required to remain above 475°C to provide >50°C salt superheat to prevent the salt from freezing within the heat exchanger. The maximum air flow rate was restricted to 10,000 CFM based on considerations of duct and blower sizes and the peak outlet air temperature. In coordination with the remainder of the loop, the predicted pressure drop around the system was restricted to two atmospheres (29.4 psid) when the salt was at the full flow rate of the salt. Finally, the design was restricted to standard tube/pipe and fin dimensions.

The final heat exchanger core design includes two rows of eight pipes for a total of 16 pipes that are 46.5 inches (1.18 m) long. Based on material sourcing and US finned tube manufacturing capabilities, the finned pipes are constructed from 1-inch schedule 40 seamless C-276 pipes (1.315 inch OD, 1.049 inch ID). The welded helical serrated fins are made of 304 stainless steel and are 0.05 inch thick, 0.17 inch wide at their tip, and 0.51 inch long, with 5 rows of fins per linear inch of pipe (Figure 10). The finned pipes are welded to tube sheets in a staggered triangular pitch pattern. The center-to-center spacing of the pipes is 2.473 inch (62.8 mm) laterally and 2.337 inch (59.4 mm) along the diagonal between the two rows of tubes. The tube sheets are welded to plenums on either side where the salt enters/exits the heat exchanger core (Figure 11a).

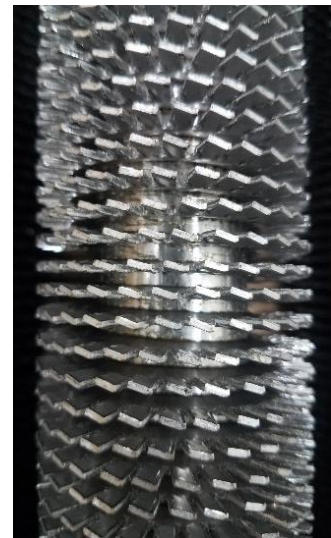


Figure 10. Finned tubing.

The heat exchanger core is supported by an insulated box that resides inside an enclosure with doors on the front and back faces. Winches can be used to lower or raise the doors to expose the heat exchanger core to forced air flow. Tubular heaters between the doors and the heat exchanger core are used to preheat the heat exchanger before salt is introduced (Figure 11b). The heat exchanger core and doors are housed within an outer enclosure to contain and direct air flow across the heat exchanger (Figure 11c). Two inches of high-temperature mineral wool insulation surround the outer enclosure to limit heat loss (Figure 12). Additional auxiliary heaters with a total capacity of 24 kW are included outside the doors, within the outer enclosure. These 480 V auxiliary heaters support preheating the enclosure and heat exchanger core. The air flow across the heat exchanger is varied via a VFD that controls a 10,000 CFM capacity blower. The blower takes suction from the roof and includes an upstream filter, a downstream damper, and a duct gate valve near the heat exchanger enclosure. The hot air from the heat exchanger is vented to a stack located on the roof through a double-walled duct with 4 inches (102 mm) of ceramic fiber insulation and a 32-inch ID.

The heat exchanger was modeled using correlations for finned tube array heat transfer [37]. Figure 13 shows design examples of the performance curves under specific conditions. Note that the required airflow indicated in the figures does not account for leaks or bypass flow around the heat exchanger.



Figure 11. Heat exchanger: (a) core, (b) inner assembly, and (c) housing assembly.



Figure 12. Insulated and installed heat exchanger assembly.

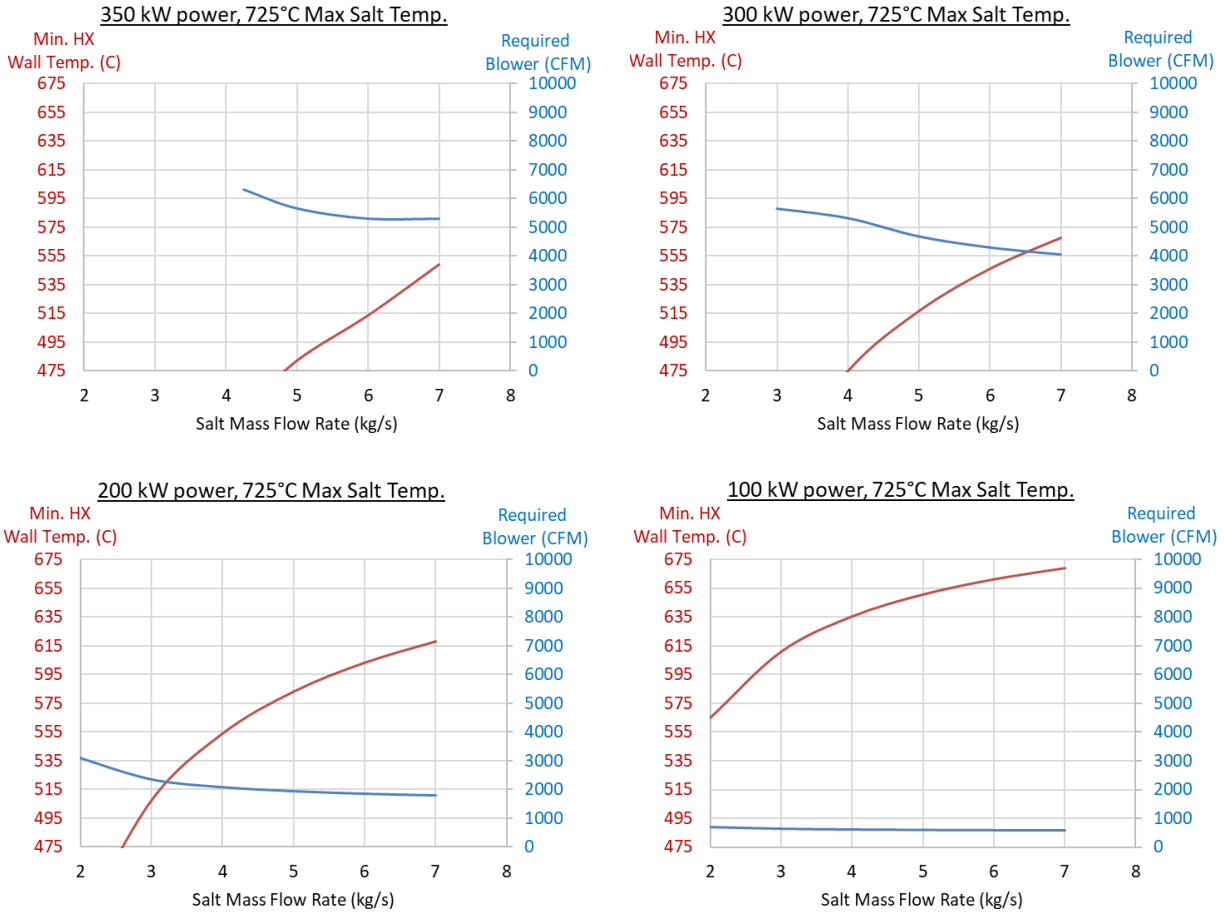


Figure 13. Example predicted heat exchanger characteristics (725°C inlet).

2.11 MAIN PIPING AND TEST PORTS

The main piping of the loop is 2-inch schedule 40 seamless C-276 pipe. Flanges that were custom developed at ORNL are included on either side of the major components—the pump tank, the main heater, and the heat exchanger—to facilitate swapping out components in the future. An additional flange is located inside the ventilated enclosure. The main heater and heat exchanger are suspended by variable spring hangers. Four hangers are used to support the main heater, and two hangers support the heat exchanger. A preliminary stress analysis of the piping network was conducted using finite element analysis (FEA) (Appendix D). This preliminary stress analysis demonstrated that the stresses are acceptable for a wide range of operating conditions.

At six locations in the piping, ports with an inner nominal diameter of 2.067 inches (52.5 mm) are included to allow for the introduction of corrosion coupons, sensors, or other experimental apparatuses (Figure 1). These include three ports on the cold side and three ports on the hot side of the loop. In addition, the pump tank includes few additional smaller ports (see Table 7). Finally, another port dedicated to managing the cover gas volume and pressure as the loop is filled/drained is located above the heat exchanger at the very top of the loop.

2.12 CORROSION SPECIMENS

Corrosion test specimens are included in the inaugural operation of the loop (Figure 14). The specimens are solid rods of alloy C-276 (0.25 in. and 0.375 in. nominal OD) and alloy 600 (0.025 in. nominal OD). The specimens are affixed to a flow diverter, which is a wedge-shaped piece of C-276 attached to a flange. An assembly is inserted vertically into a wye in the main piping. The flow diverter is aligned in the wye to divert the majority of the flow toward the desired flow path and away from flange. One assembly of the three specimens is located above the main heater on the hot side of the loop, and another assembly is located on the cold side of the loop. After exposure, the assemblies will be removed, sectioned, and analyzed for corrosion.

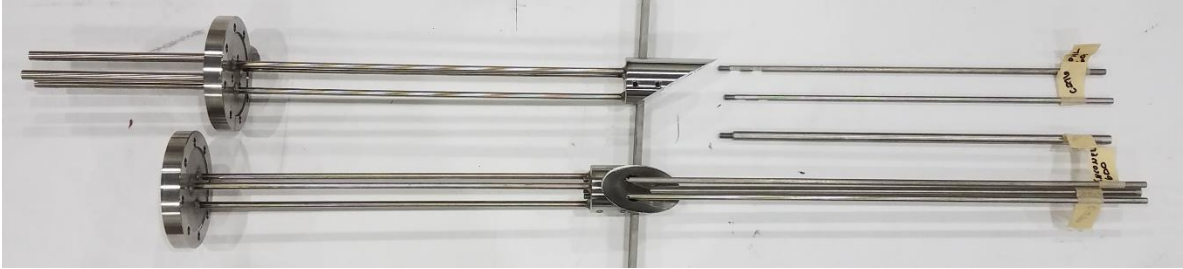


Figure 14. Corrosion specimen assemblies.

2.13 INSTRUMENTATION

The piping and instrumentation diagram in Figure 15 identifies the piping layout and the general location of instrumentation.

2.13.1 Temperature

Standard type N thermocouples are placed externally throughout the system to measure temperature. The quantities and general locations of thermocouples are summarized in Table 2 and are illustrated in Figure 15. Temperature measurements in the salt are taken via the salt-level probes (Section 2.13.5).

2.13.2 Hazardous Gas Sensors

Cl₂, HCl, H₂, and/or other hazardous gases could be generated during purification, loop operation, and or during off-nominal events like air-ingression or outward leakage. To detect the presence of Cl₂, HCl, or H₂, five Honeywell Midas T-004 gas sensors are distributed around the facility. Two are located inside the enclosure, and three are outside the enclosure.

2.13.3 Salt Flow Rate

An ultrasonic flow meter manufactured (Flexim, Inc.) is used to measure the salt flow rate. This flowmeter is similar to that used on the LSTL [36]. The Flexim WaveInjector meter was designed specifically to operate at a loop temperature of 700°C. Wave guides were designed to ensure that the piezoelectric transducers remain at a safe operating temperature. Metal clamps attach the flow meter wave guides to the pipe's surface. These metal clamps and wave guides pose a thermal management challenge with respect to maintaining the pipe temperature above the salt freezing point while maintaining the piezoelectrics below their safe operating temperature. A heater and insulation solution that was developed for temperature control on the LSTL was also used for FASTR to regulate component temperatures. The flow meter is attached to the cold side of the loop between the heat exchanger and the pump tank. This

length of pipe will allow for approximately 24 pipe diameters of development length before the flow meter and 9.5 pipe diameters after the flow meter.

2.13.4 Salt Chemistry

To monitor the state of the salt, multifunctional voltammetry sensors were developed at Argonne National Laboratory (ANL) [44] for inclusion in the loop. The sensors can detect the salt redox potential and the concentration of Mg, some oxide impurities, and key metallic species. Online detection of changes in specie concentrations and/or redox potential will serve to indicate corrosion or air/moisture ingress and will be used to help determine the need for corrective actions. Two of the sensors are located in test ports on the loop to monitor the salt redox potential and the concentration of specific species. These sensors are capable of measuring liquid level. Two more simplistic sensors are included in the purification vessel and storage tank.

2.13.5 Salt Level

The salt level is monitored using heated thermocouple arrays that are located inside the storage tank, in the pump tank, in the top vent port, and inside one test port. Each array consists of five thermocouples and a heater wire inside an alloy 600 sheath. The spacing between thermocouples vary either 1.5 or 2.0 inches. A pair of arrays is inserted into a given component. The heater wire of one of the two arrays is heated. The temperatures of the thermocouples below the salt surface are lower than the temperatures of the thermocouples in the gas space because of the differences in heat transfer. The second array, which is unheated, is used to measure and correct for axial temperature gradients in the salt and gas space. The salt level can be predicted by comparing the temperatures of the heated and unheated thermocouple arrays. This technique can only detect whether the salt level is between two discrete thermocouple elevations. The salt level can also be deduced from the multifunctional voltammetry sensor measurements.

2.13.6 Gas Pressure and Salt Level Control

The gas pressure is measured and controlled at several locations (Table 8). The gas pressure is measured with standard pressure transducers (Honeywell model FP2000). A set of in- and out-flow MFCs (MKS model GE50A) can add or remove gas to the space. Filters (7 μm nominal apertures, 1280 mm^2) are placed upstream of the out-flow MFCs to capture particulate that could foul the MFCs. An additional solenoid valve on the pump tank facilitates more rapid depressurization and draining of the salt loop piping. The operators can set a manual flow rate, or they can specify a target pressure, and the MFC will adjust accordingly. Several relief valves are located throughout the system as shown in Table 9. The relief setpoints are based on corresponding tank design.

Table 8. Gas mass flow controller and pressure transducer sizes

Location	Maximum flow rate (SLPM)	Pressure transducer maximum (psig)
Flanges (in and out)	0.200	50
Top gas vent (in and out)	10	50
Test port (in and out)	10	50
Storage tank (in and out)	50	50
Pump tank (in and out)	50	50
Process vessel (sweep line)	5	30
Process vessel (bubbler line)	5	30

Table 9. Pressure relief locations and setpoints

Location	Relief setpoint (psig)
Gas supply panel	90
Processing vessel	30
Storage tank	30
Pump tank	21.5

2.14 CONTROL SYSTEM AND TRACE HEATING SUMMARY

The data acquisition and control system is driven by an Allen Bradley 1756 PLC containing various input and output modules for data acquisition and control. Two cabinets house Allen Bradley 1794 FLEX I/O thermocouple input modules. The thermocouple data are passed to the main PLC via ethernet modules.

Three custom heater control cabinets were designed and fabricated at ORNL. Each heater control cabinet comprises 16 controllable heater zones, for a total of 48 total zones. Each zone includes a relay controlled via the PLC, and upstream of each relay is a breaker. In the main heater (described in Section 2.9) 6 additional heater zones are controlled by a separate control system that interfaces with the main PLC.

The processing vessel, storage tank, and pump tank are wrapped in heater blankets which include embedded heaters with surrounding insulation. Other locations use tubular heaters and/or cartridge heaters. Finally, heat tapes of various sizes are used to supply trace heating to tubing and piping throughout the loop and transfer lines. Table 10 summarizes the trace heating locations and maximum powers.

Table 10. Heater summary

Component	Location	Max power^a (W)
Processing vessel	Upper	3,600
	Middle	3,600
	Lower	2,400
	Bottom	1,590
Storage tank	Upper	1,783 × 2
	Middle	734 × 2
	Lower	1,081 × 2
Pump tank	Upper	1,000
	Middle	1,750
	Lower	1,750
	Bottom	1,500 × 2
Main heater	Top plenum	500 × 2
	Bottom plenum	500 × 2
	Top face temporary	936 × 2
	Bottom face temporary	1,248 × 2
Heat exchanger	Top plenum	600 × 2
	Face top	1,750 × 2
	Face bottom	1,750 × 2
	Bottom plenum	600 × 2
Transfer tube	Auxiliary	4,000 ^b × 6
	2 zones	1,248 × 2
Loop piping	27 zones	~26,100 distributed

^a Based on 240V

^b Based on 480V

3. LOOP OPERATING MODES AND CAMPAIGNS

3.1 PREDICTED THERMAL-HYDRAULIC OPERATING ENVELOPE AND CONDITIONS

The actual operating envelope will be determined during the system startup phase. However, the loop operation envelope is constrained to the following conditions:

- Salt temperature (500–725°C)
- Salt temperature differential (0–100°C)
- Loop main-heat addition/rejection (0–350 kW_{th})
- Salt flow rate (3–7 kg/s)

The flow loop was modeled to predict the system pressure drop, the heat exchanger, and the main heater characteristics using analytical and semi-empirical techniques. The spreadsheet model and supplemental higher fidelity analyses of the heat exchanger and main heater were used to size components and predict the potential operating envelope for the system. There are uncertainties in salt thermophysical properties and in the correlations used for pressure drop and heat transfer.

Pressure losses were modeled around the flow loop for isothermal conditions, as seen in Figure 16. Form loss (i.e., K coefficient) was modeled as 0.45 for pipe bends and 1.4 for combined contraction-expansion losses (e.g., inlet and outlet of heat exchanger tubes). The salt thermophysical properties were taken as those for KCl-MgCl₂ [38]. The results shown in Figure 16 indicate that the pressure drop is not sensitive to the salt temperature.

To keep the heat exchanger tube's surface temperature above 475°C—a self-imposed limit to ensure that salt does not freeze in the channels—the maximum main heater power is given in Figure 17. For a given curve, areas under the curve are feasible operating conditions, whereas areas above the curve are predicted to have tube surface temperatures below 475°C. Manipulating the heat exchanger doors and/or the use of trace heating may expand the operational envelope.

Based on a constant specific heat of 1,150 kJ/kg-K, the salt temperature difference between the hot and cold sides of the loop is presented in Figure 18. A steady-state temperature difference up to 100°C is attainable based on a 3 kg/s flow rate. However, as shown in Figure 17, the maximum power at 3 kg/s may be 230 kW based on heat exchanger limits.

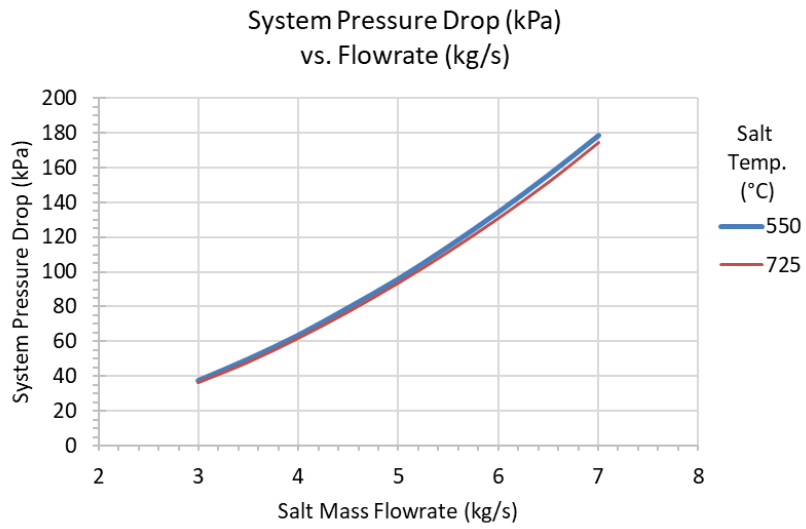


Figure 16. Predicted pressure drop vs. mass flowrate.

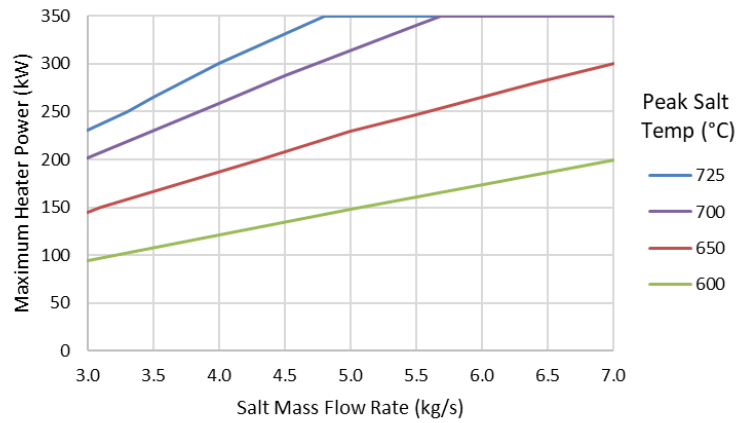


Figure 17. Maximum heater power at various maximum salt temperatures based on heat exchanger limits.

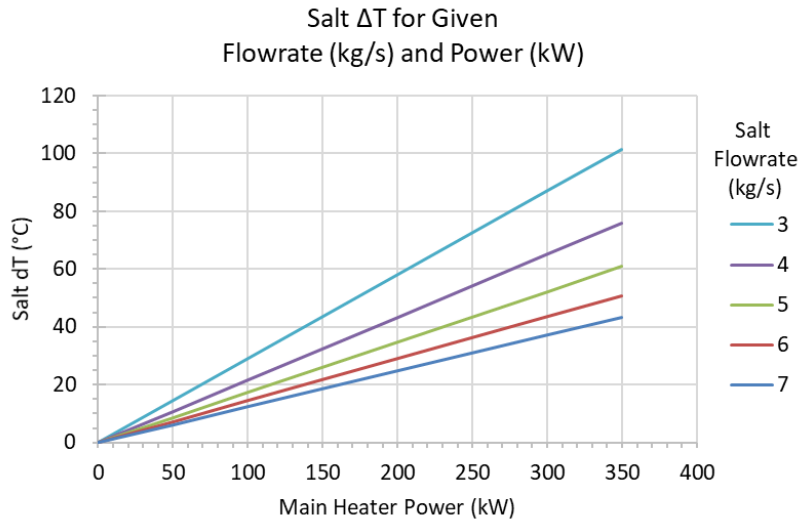


Figure 18. Salt ΔT based on flowrate and main heater power.

3.2 PLANNED TEST CAMPAIGNS

An initial test plan, shown in Table 11, covers the shakedown testing of the installed system, determination of the system characteristics and operation envelope, and the testing to be completed to obtain the scientific data needed to guide future molten salt technology development.

As operational experience is accumulated, system operation logistics will progress. Initially, FASTR will be staffed and monitored during normal business hours. During off-normal hours, the system will be placed in hot standby with the pump disabled and the loop drained. As more experience is gained, FASTR will progress towards the goal of operating the loop without having staff locally present—first during normal business hours, and eventually during off-normal hours. This progression will depend on system performance, as well as experience and input from environment, health, and safety personnel and other stakeholders.

Table 11. Initial test plan.

Phase: Shakedown	
Purpose: ensure that subcomponents meet performance expectations before salt introduction	
I&C verification	Verify temperature, gas pressure, gas flowrate sensor readings
Heater operation	Verify individual heater integrity
Pump operation dry	Run dry, take up to speed, and balance as needed
Heat exchanger operation	Verify fan operation
System leak check (gas, room temperature)	Leak check fittings, flanges, etc., at low temperatures
Heat system: isothermal	Ensure the ability to maintain system temperatures; estimate heat losses
System leak check (gas, high temperature)	Leak check fittings, flanges, etc., at high temperatures
System trips	Verify preset system trips to the extent possible
Pump operation wet	Run system with water and verify pump operation and system controls
Phase: Startup	
Purpose: (1) characterize integral system behavior, and (2) determine the system operational envelope	
Salt characterization	Perform baseline measurements of salt composition, impurities, electrochemical potential
I&C verification	Verify flow rate, pressure, level sensor, and electrochemical sensor readings
Isothermal operation	Ensure the ability to maintain system temperatures while salt is flowing; estimate zone heat losses
Heater performance	Verify heat transfer vs. input power for salt flow rate (3–6 kg/s) and inlet temperature (500–700°C)
Pump performance	Verify pump curve to system capabilities (3–6 kg/s)
Heat exchanger performance	Verify heat transfer vs. fan speed and door location for salt flow rate (3–6 kg/s), inlet temp. (525–725°C)
System trips	Revise preset system trips based on the operational envelope
Phase: Test Campaigns	
Purpose: Obtain quality scientific data	
Corrosion control demonstration	Conduct coupon tests: 2 × lines (1 × hot leg, 1 × cold leg) of 12 samples (6 × C-276, 6 × Inconel 600); conducted over 100 h and 200 h In-situ corrosion measurement (as applicable)
Heat transfer in main heater and heat exchanger	Test heat transfer vs. fan speed, salt flow rate (3–6 kg/s) Reynolds number (15,000–50,000), salt inlet temp (500–700°C)
REDOX control system and oxygen/impurity sensors demonstration	Demonstrate reduction and control of oxygen/impurities using the REDOX control system as applicable (e.g., getter can, electrochemical oxygen removal). This testing will occur over the course of other planned tests and could include intentional introduction of impurities.
Extended operation demonstration	Demonstrate robustness of system through extended runs with salt circulating in the system >500°C and a >25°C temperature gradient.

3.3 POTENTIAL TEST CAMPAIGNS

Several technologies require development and demonstration to de-risk molten salt systems. Although a thorough review of each need is beyond the scope of this report, the following subsections highlight several areas in which FASTR could be utilized to advance high-temperature molten salt technology.

3.3.1 Salt-to-sCO₂ Heat Exchangers

Future high-temperature molten salt systems are envisioned to be coupled with supercritical carbon dioxide (sCO₂) power cycles. At the heart of that integrated systems is a salt-to-sCO₂ heat exchanger. This component operates under severe service conditions with high-pressure sCO₂ on one side and low-pressure salt on the other while remaining at high temperature with substantial temperature gradients. Printed circuit heat exchangers (PCHEs) are a compact solution being developed for extension into this application space. Recent efforts and advances have been made in diffusion bonding applicable alloy plates that comprise the PCHE.

Demonstrating a PCHE at a relevant scale with respect to bonding is of interest to de-risk and demonstrate this key component. While some separate effects tests can be conducted, a demonstration requires the coupling of a molten salt facility and an sCO₂ loop. This objective motivated an initial effort to investigate conducting relevant testing at FASTR.

The PCHE would be attached to FASTR in-line inside the ventilated enclosure under the heat exchanger. There is already one flange in the piping in this location. The ventilated enclosure would capture any gaseous leakage from the PCHE and would contain more severe failures. A sCO₂ loop would be built external to the enclosure and abutted against the side door. A sCO₂ loop was designed to test a 100 kW_{th} scale PCHE.

3.3.2 Salt Valves

The performance and reliability valves for salt service is a recognized component challenge. The current FASTR configuration intentionally excluded salt valves at the onset of the project because of the known costs, schedule, and technical risks. The Gen3 CSP liquid pathway pilot plant project included a topical effort to advance and de-risk valves. For that effort, an alloy C-276 valve was sourced, and plans were developed to test the valve in FASTR. The valve would be located near the discharge of the pump in the region below the main heater. A custom heater jacket for the valve was also designed and procured. Initial designs for the valve support and the required I&C were developed. Because of project timing, alternate arrangements were pursued for the testing the valve, but salt valves remain on the list of key components to be demonstrated.

3.3.3 Instrumentation

Salt flow meters and salt-wetted pressure transducers are two notable instrumentation challenges. Solutions exist, but demonstration and calibration of such instrumentation is needed. FASTR includes custom electrochemical sensors developed by ANL that provide unprecedented in-situ monitoring of the salt chemistry. These and similar instruments must be demonstrated for extended periods in flowing systems.

3.3.4 Off-Gas and Vapor Pressure Effects

The vapor pressure of the salt may have deleterious impacts on loop operation. These challenges may be exacerbated in larger, more complex facilities. Developing and demonstrating techniques to monitor and

mitigate vapor pressure effects would further de-risk implementation of high-temperature chloride salt systems.

3.3.5 Purification Processes and Online Redox Control

The initial salt purification was successful and is discussed in the literature [43]. The available infrastructure could be leveraged to test other purification process (e.g., time, temperature, flow rates, initial preparation, filtering, different reagents, off-gas handling scheme).

The online control of the salt redox potential is an area for further refinement. Contacting the salt with metallic Mg may prove successful. Automation and implementation of this control scheme in the hot flowing salt remains to be demonstrated.

3.3.6 Digital Model Validation Testbed

Recent advancements in modeling and simulation, as well as unique monitoring and control schemes, have been significant. The FASTR loop may provide experimental data to validate modeling efforts (e.g., computation fluid dynamics), or it may serve as a test-bed for modern sensing and control architectures (e.g., digital twins).

3.3.7 Handling, Operations and Maintenance

FASTR is one of very few >100 kg scale high-temperature molten salt facilities in the United States. Halide molten salts have a relatively high melting point and strict hermeticity requirements, thus presenting unique handling, operation, and maintenance challenges. FASTR could be used to inform the operation and maintenance procedures for future facilities, and it also serves as a venue for gaining hands-on experience operating a large forced flow salt system.

4. CONCLUDING REMARKS

FASTR is a state-of-the-art molten chloride salt facility with appreciable pumping capacity, thermal power, and temperature capabilities. With respect to scale, along with the Integral Effects Test [45] which is planned to become operational in 2022, FASTR currently represents the largest and most capable high-temperature chloride salt test loop in the United States. The project was initiated in parallel with the development of the fundamental understanding of molten chloride salts, including composition selection, thermophysical properties, salt preparation methodology, chemistry control scheme, and material compatibility. Early project decisions (e.g., material selection, purification process and infrastructure, assumed properties) have been supported by findings from this parallel research. Sourcing of custom high-nickel alloy parts and the impacts of the 2020 global COVID-19 pandemic were notable challenges to the execution of the loop. However, the early choice of C-276 remains valid based on continued compatibility studies, and the system was successfully constructed. While new findings from loop operations are anticipated, at its current stage, the facility represents a major step in the advancement and de-risking of high-temperature chloride salt technology.

5. REFERENCES

1. M. Mehos et al., *Concentrating Solar Power Gen3 Demonstration Roadmap*. National Renewable Energy Laboratory (NREL), Golden, Colorado, 2017.
2. Kenneth Miguel Armijo et al. *Operational Modes of a 2.0 MWth Chloride Molten-Salt Pilot-Scale System*. SAND2019-10294C. Sandia National Laboratories (SNL-NM), Albuquerque, NM (United States), 2019.
3. Kenneth Miguel Armijo et al. *Operational Modes and System Design of a 2.0 MWth Sodium-Molten Salt Pilot System*. SAND2019-15260C. Sandia National Laboratories (SNL-NM), Albuquerque, NM (United States), 2019.
4. K. R. Robb, *Simplified High-Temperature Molten Salt CSP Plant Preconceptual Design*, Oak Ridge National Laboratory, ORNL/TM-2022/2377, March 2022.
5. K. R. Robb, P. Mulligan, G. Yoder, Jr., K. Smith, and J. Massengale, *Facility to Alleviate Salt Technology Risks (FASTR): Preliminary Design Report with Failure Modes and Effects Analysis*, Oak Ridge National Laboratory, ORNL/TM-2019/1370, 2019.
6. Haynes International, "HASTELLOY® C-276 alloy," Pub. ID H-2002E, <http://haynesintl.com/docs/default-source/pdfs/new-alloy-brochures/corrosion-resistant-alloys/brochures/c-276.pdf>
7. Special Metals Corporation, "INCONEL® Alloy C600," Pub. ID SMC-027, <https://www.specialmetals.com/assets/smc/documents/alloys/inconel/inconel-alloy-600.pdf>
8. H. Sun, J. Wang, Z. Li, P. Zhang, and X. Su. "Corrosion Behavior of 316SS and Ni-Based Alloys in a Ternary NaCl-KClMgCl₂ Molten Salt," *Solar Energy* 171, 320–329, 2018.
9. Sun, Hua, Peng Zhang, and Jianqiang Wang. "Effects of Alloying Elements on the Corrosion Behavior of Ni-Based Alloys in Molten NaCl-KCl-MgCl₂ Salt at Different Temperatures." *Corrosion Science* 143, 187–199, 2018.
10. K. Vignarooban, et al., "Corrosion Resistance of Hastelloys in Molten Metal-Chloride Heat-Transfer Fluids for Concentrating Solar Power Applications," *Solar Energy* 103, 2014.
11. Xiankun Xu et al., "Experimental Test of Properties of KCl-MgCl₂ Eutectic Molten Salt for Heat Transfer and Thermal Storage Fluid in Concentrated Solar power Systems," *Journal of Solar Energy Engineering* 140, 2018.
12. Rishi Pillai, Stephen S. Raiman, and Bruce A. Pint. "First Steps toward Predicting Corrosion Behavior of Structural Materials in Molten Salts." *Journal of Nuclear Materials* 546, 2021, 152755.
13. Wenjin Ding et al., "Molten Chloride Salts for Next Generation Concentrated Solar Power Plants: Mitigation Strategies against Corrosion of Structural Materials." *Solar Energy Materials and Solar Cells* 193, 298–313, 2019.
14. Mohammad Alkhamis, "Stability of Metal in Molten Chloride Salt at 800 C," MS dissertation, University of Arizona, 2016.
15. W. Ren, K. Robb, "Selection of Alloy C-276 and Extension of Its Code Design Values for Advanced Molten Salt Technology Test Facilities Experimentation," Proc. ASME 2020 Pressure Vessels & Piping Division Conference (PVP2020), July 19–24, 2020, Minneapolis, MN.
16. R. Mayes, J. M. Kurley, III, A. McAlister, D. Sulejmanovic, S. S. Raiman, B. A. Pint, P. W. Halstenberg, and S. Dai, *Purification of Chloride Salts for Concentrated Solar Applications*, ORNL/LTR-2018/1052. Oak Ridge National Laboratory, 2019.

17. J. M. Kurley, III, et al., “Enabling Chloride Salts for Thermal Energy Storage: Implications of Salt Purity,” *RSC Adv.* 9, pp. 25602–25608, 2019.
18. C. J. Raseman, H. Susskind, G. Farber, W. E. McNulty, and F. J. Salzano, *Engineering Experience at Brookhaven National Laboratory in Handling Fused Chloride Salts*, BNL-627, Brookhaven National Laboratory, 1960.
19. T. R. Johnson, F. G. Teats, and R. D. Pierce, *A Method for the Purification of Molten Chloride Salts*, ANL-7603, Argonne National Laboratory, 1969.
20. Hill, Derek L., Jeanne Perano, and Robert A. Osteryoung. “An Electrochemical Study of Uranium in Fused Chlorides.” *Journal of The Electrochemical Society* 107.8 (1960): 698.
21. J. W. Ambrosek, “Molten Chloride Salts for Heat Transfer in Nuclear Systems,” PhD Dissertation, The University of Wisconsin - Madison, 2011.
22. Y. Zhao, and J. Vidal. “Potential Scalability of a Cost-Effective Purification Method for MgCl₂-Containing Salts for Next-Generation Concentrating Solar Power Technologies.” *Solar Energy Materials and Solar Cells* 215, 2020.
23. B. L. Garcia-Diaz, L. Olson, M. Martinez-Rodriguez, R. Fuentes, H. Colon-Mercado, J. Gray, “High Temperature Electrochemical Engineering and Clean Energy Systems,” *Journal of the South Carolina Academy of Science*, 14(1), 4, 2016.
24. B. L. Garcia-Diaz, *Fundamental Corrosion Studies in High-Temperature Molten Salt Systems for Next Generation Concentrated Solar Power Systems*, SRNL-STI-2019-00017. Savannah River Site, Aiken, SC, 2016. doi:10.2172/1491796.
25. B. A. Pint, J. W. McMurray, A. W. Willoughby, et al., “Re-Establishing the Paradigm for Evaluating Halide Salt Compatibility to Study Commercial Chloride Salts at 600–800°C,” *Materials and Corrosion* 70, 1439–1449, 2019.
26. Bruce A. Pint, *Progression to Compatibility Evaluations in Flowing Molten Salts*. ORNL/SPR-2020/1490. Oak Ridge National Laboratory, Oak Ridge, TN (United States), 2020.
27. Brendan Harry D’Souza, “Material Degradation Studies in Molten Halide Salts.” Dissertation, Virginia Tech, 2021.
28. Brendan D’Souza et al. “Impurity Driven Corrosion Behavior of HAYNES® 230® Alloy in Molten Chloride Salt.” *Corrosion Science* 187, 2021, 109483.
29. Brendan D’Souza et al. “Corrosion Behavior of Boronized Nickel-Based Alloys in the Molten Chloride Salt.” *Corrosion Science* 182, 2021, 109285.
30. James R. Keiser et al. “Material Selection and Corrosion Studies of Candidate Bearing Materials for Use in Molten Chloride Salts.” *Journal of Solar Energy Engineering*, 1–12, (2022).
31. Qi Lui et al. “Ni-Mo-Cr Alloy Corrosion in Molten NaCl-KCl-MgCl₂ Salt and Vapour.” *Corrosion Science* 180, 2021, 109183.
32. Qi Liu et al. “Corrosion Behaviour of 316 Stainless Steel in NaCl-KCl-MgCl₂ Salt Vapour at 700°C.” *Corrosion Science* 194, 2022, 109921.
33. B.C Kelleher, S.F. Gagnon, and I.G. Mitchell. Thermal Gradient Mass Transport Corrosion in NaCl-MgCl₂ and MgCl₂-NaCl-KCl Molten Salts.” *Materials Today Communications*, 2022, 104358.
34. Hua Sun et al. “Assessment of Effects of Mg Treatment on Corrosivity of Molten NaCl-KCl-MgCl₂ Salt with Raman and Infrared Spectra.” *Corrosion Science* 164, 2020, 108350.

35. G. L. Yoder, Jr., et al., "An Experimental Test Facility to Support Development of the Fluoride-Salt-Cooled High-Temperature Reactor." *Annals of Nuclear Energy* 64: 511–517, 2014.
36. G. L. Yoder, Jr., A. M. Aaron, R. B. Cunningham, D. L. Fugate, D. E. Holcomb, R. A. Kisner, F. J. Peretz, K. R. Robb, and D. F. Wilson, *High Temperature Fluoride Salt Test Loop*, ORNL/TM-2012/430, Oak Ridge National Laboratory, 2015.
37. S. Kalac, R. K. Shah, and W. Aung, *Handbook of Single-Phase Convection Heat Transfer*, Chapter 6, John Wiley and Sons, 1987.
38. M. Sohal, *Engineering Database of Liquid Salt Thermophysical and Thermochemical Properties*, INL/EXT-10-18297, 2010.
39. Special Metals Corporation, "INCONEL® alloy C-276," Pub. ID SMC-019, <https://www.specialmetals.com/assets/smc/documents/alloys/inconel/inconel-alloy-c-276.pdf>
40. D.F. Williams, *Assessment of Candidate Molten Salt Coolants for the NNGNP/NHI Heat-Transfer Loop*, ORNL/TM-2006/69. Oak Ridge National Laboratory, , 2006.
41. Xiaoxin Wang et al. "Thermophysical Properties Experimentally Tested for NaCl-KCl-MgCl₂ Eutectic Molten Salt as a Next-Generation High-Temperature Heat Transfer Fluids in Concentrated Solar Power Systems." *Journal of Solar Energy Engineering* 143.4 (2021): 041005.
42. N. Goth, T. Nguyen, K. Robb, and E. Kappes, "Numerical Investigation of Cartridge Heater Performance Applied to the FASTR Main Heater for Molten Chloride Salts," *Proc. of 2022 American Nuclear Society Annual Meeting*, Anaheim, CA, June 12–16, 2022.
43. K. R. Robb, S. Baird, J. Massengale, N. Hoyt, J. Guo, and C. Moore, *Engineering-Scale Batch Purification of Ternary MgCl₂-KCl-NaCl Salt Using Thermal and Magnesium Contact Treatment*, ORNL/TM-2022/2554, Oak Ridge National Laboratory, 2022.
44. J. Guo, N. Hoyt, and M. Williamson. "Multielectrode Array Sensors to Enable Long-Duration Corrosion Monitoring and Control of Concentrating Solar Power Systems." *Journal of Electroanalytical Chemistry* 884, 2021.
45. Press release, "Southern Company and TerraPower Prep for Testing on Molten Salt Reactor," <https://www.energy.gov/ne/articles/southern-company-and-terrapower-prep-testing-molten-salt-reactor>, accessed May 2022.

APPENDIX A. FACILITY INDIVIDUAL SHAKEDOWN CONFIGURATION

An alternate configuration was explored in which a pipe bypasses the heat exchanger to enable early operation of the facility. The FASTR-Individual Shakedown (FASTR-ISH) configuration is illustrated in Figure A.1. Bypassing the heat exchanger greatly reduces the amount of heat the loop can reject. This results in a lower achievable temperature gradient across the hot-side and cold-side of the loop. However, the configuration enables operation of the pump, main heater, and other supporting operations. The bypass pipe was fabricated, but the configuration was not installed or operated.

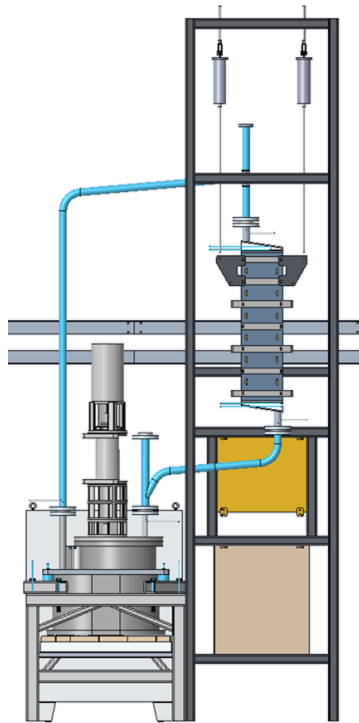


Figure A.1. FASTR-Individual Shakedown configuration.

APPENDIX B. MAIN HEATER FINITE ELEMENT ANALYSIS

After optimizing part dimensions by modeling a representative subsection of the heater plate, work was performed to understand the temperature evolution and maximum deformation in the entire component under typical operating conditions. A full-scale computer aided design rendering of the heater plate was modeled using ANSYS finite element analysis (FEA) software assuming axial symmetry through the plate thickness and width. User-defined heat fluxes were applied to six heaters composed of aluminum nitride along the length of the plate to simulate the planned six-zone independent heating configuration. Two inches of high-temperature block insulation were placed over the AlN heaters to minimize heat loss to the ambient atmosphere. Thermal convection coefficients and bulk temperatures for each salt channel were modeled as user-defined variables to allow for exploration of any loop operating condition. The range of values for heat flux, bulk temperature, and coolant heat transfer coefficient used in the FEA model are listed in Table B.1.

Table B.1. Limiting boundary conditions modeled in full scale heater plate FEA model

	Applied heat flux (W/m ²)	Salt bulk temperature (°C)	Salt channel heat transfer coefficient (W/m ² -K)
Minimum	2.08×10^5	550	1.49×10^4
Maximum	6.25×10^5	725	3.39×10^4

B.1 FEA THERMAL RESULTS

FEA models with various boundary conditions were analyzed to gain more understanding of temperature distributions and peak temperatures in the heater plate assembly. Figure B.1 depicts the temperature distribution with a linearly decreasing heat flux applied to each heater zone, with Zone 1 using the highest value from Table B.1 and Zone 6 using the lowest. Assuming a 725°C salt bulk temperature and a 14,900 W/m²-K heat transfer coefficient, temperatures reached a maximum of 967°C in the plate and 1,000°C in the heating element. Future work may include coupling this FEA model to a fluid dynamics model with chloride salt properties to gain a better understanding of loop heat transfer characteristics.

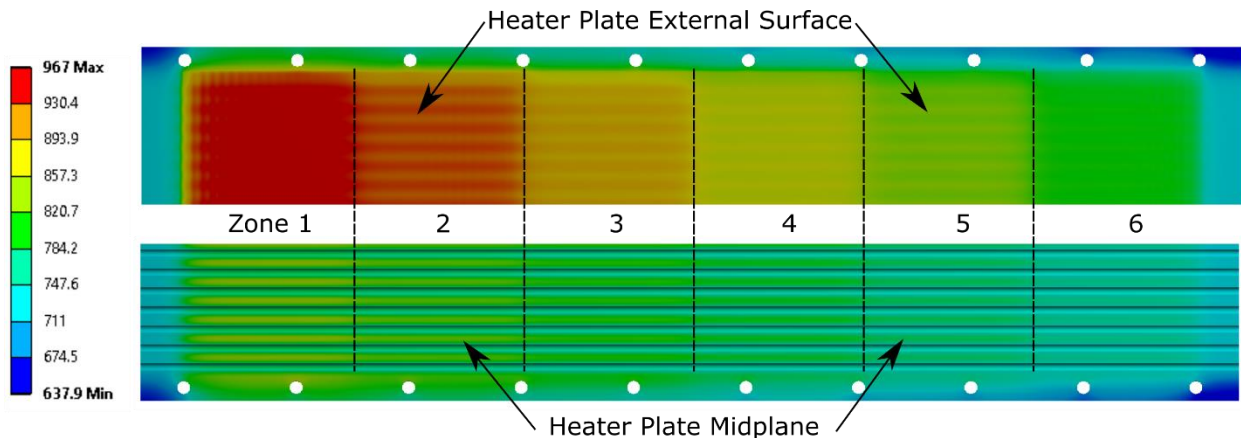


Figure B.1. Heater plate temperature distributions for linearly decreasing heat flux (from left to right).

B.2 STRUCTURAL RESULTS

Structural deformation in the plate under a range of operating conditions was analyzed by applying results of the ANSYS thermal solution to a structural simulation of the heater plate. Results of this analysis show a maximum deformation of 1.96 cm along the length of the plate, 0.4 cm laterally, as well as a 0.74 mm increase in plate thickness. This analysis has informed the design of other support components in the heater plate assembly.

APPENDIX C. PUMP SUMP TANK ANALYSIS

A finite element analysis (FEA) was conducted on the FASTR pump tank assembly using ANSYS version 19.0 engineering simulation design software. Stresses were analyzed using the expected structural and thermal loads and compared to the tank material's allowable stress at a temperature of 700°C. The computer aided design geometry was originally created in Creo/Parametric 3D modeling software. A STEP file of this solid model was exported from Creo/Parametric and imported into ANSYS. ANSYS was used to simplify the geometry, create a mesh, and apply the appropriate thermal/structural loads and boundary conditions.

C.1 FEA MESH

Meshing was developed using ANSYS's automatic meshing tool. The resulting mesh consists of 845,618 tetrahedral elements with a 0.4 inch maximum side length. The meshed model is shown in Figure C.1, Figure C.2, and Figure C.3 below. A mesh refinement (Figure C.3) was created in the reinforced section of the vessel where the higher stress was observed.



Figure C.1. Finite element model mesh.

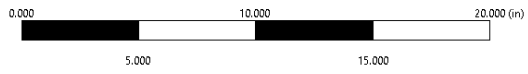
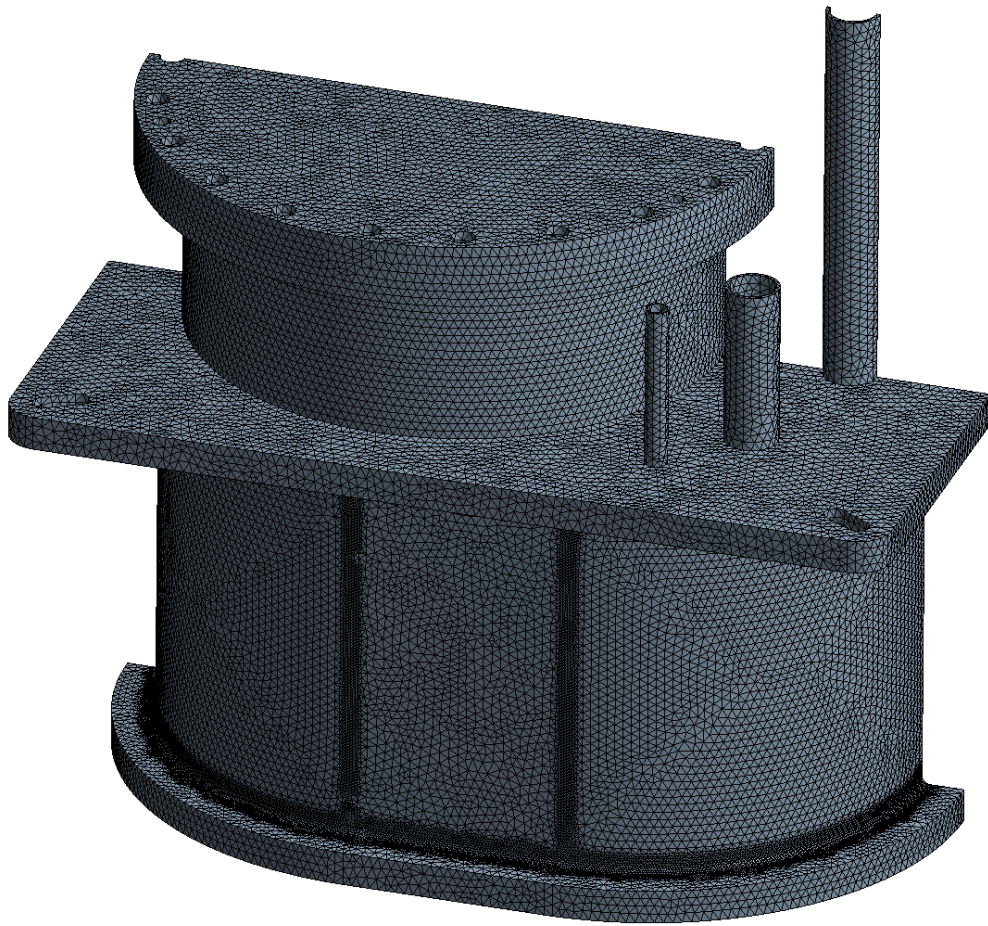


Figure C.2. Finite element model mesh.

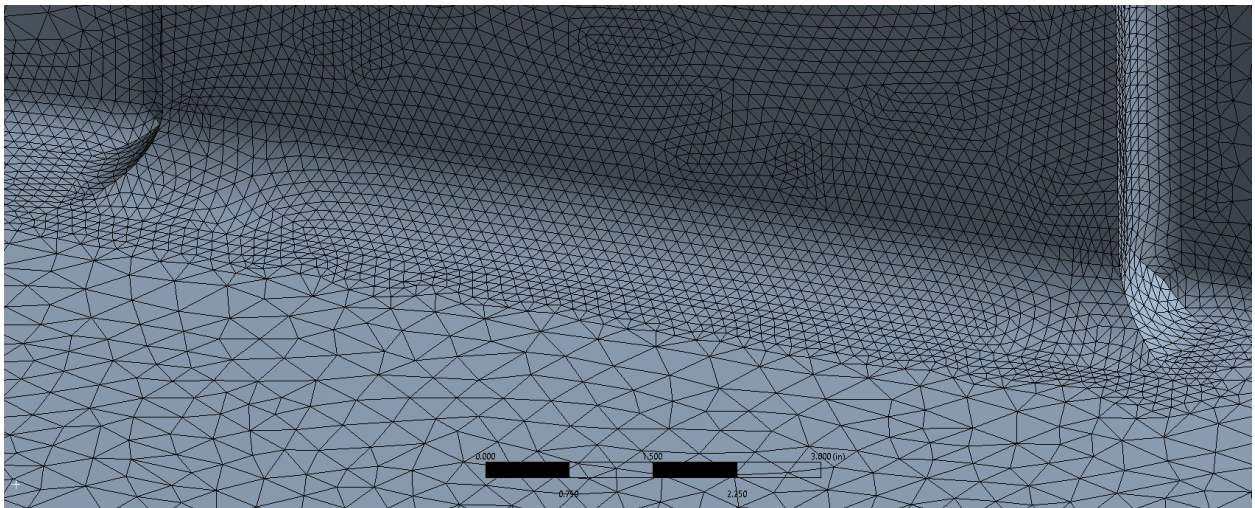


Figure C.3. Finite element model mesh.

C.2 MODEL SIMPLIFICATIONS

The model was simplified from a full 3D geometry to a 3D planar-symmetric model with symmetry specified through the XY plane. The tank is sectioned along this plane in Figure C.1. The simplification assumes that the differences in the pipe and tube sizes on the lid will have a negligible impact on the resulting stresses. The flanges on the pipe ends and the flow diverter plates that rest on the bottom of the vessel were removed from the model. Additionally, individual parts were assumed to be fully bonded at the part interfaces where welds and bolted connections are present.

C.3 FEA BOUNDARY CONDITIONS AND LOADS

The tank lid is vertically supported by four 3.5-inch diameter pads, and 0.90-inch pins secure the tank laterally in slots. The slots allow for the vessel to have unconstrained lateral motion in the direction of the slot when the tank expands and contracts during heating and cooling cycles. These supports are shown in the Creo model in Figure C.4.

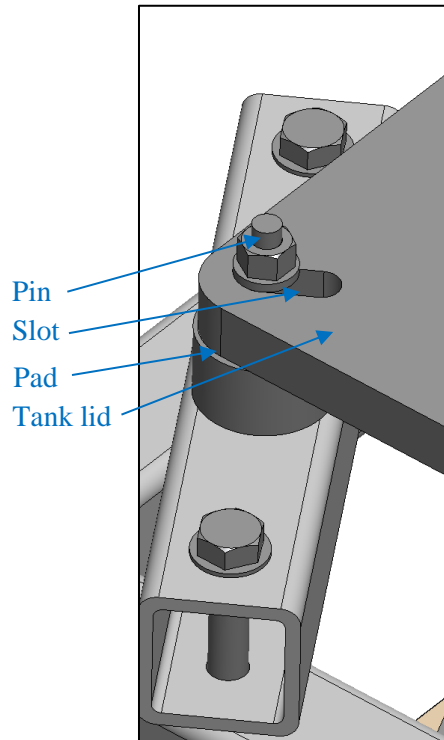


Figure C.4. Pump tank supported by pad and pin.

The pads are simulated in ANSYS, with circular cosmetics and frictionless supports applied to these regions. These boundary conditions are shown in blue in Figure C.5. The lateral constraint is represented by assigning a frictional contact to the vertical surface of a slot as shown in green in Figure C.6.

A pump and motor assembly will be mounted to the blank flange depicted at the top of the tank assembly. This pump assembly is simulated in the ANSYS model by applying a pressure load across the top surface of the flange in the vertical direction. The pump vendor estimated the weight of the pump to be 1,000 lb, so a force of 1,000 lbf was applied in the simulation. This load is depicted below in Figure C.7.

For the results shown in Section C.5, the tank was modeled with a 21.5 psig internal pressure. The pressure is applied to all inside surfaces of the pump tank. The pressure is applied as normal to the

selected surfaces highlighted in red in Figure C.8. As shown below in Section C.6, the tank pressure was varied parametrically from 0 to 30 psi.

Standard Earth gravity of 386.09 in/s² is applied to the model. A thermal condition of 700°C is assigned to all bodies. No thermal gradients in the structures were modeled. The loads and thermal condition are applied in a stepwise fashion, with the thermal load being applied before the structural loads are applied.

In the reinforced section-to-tank shell interfaces, 3/4-inch corner radii were added to simulate fillet weld geometry, as shown in Figure C.9. The purpose of the fillets is to provide a more accurate understanding of the stresses in this region. The lower portion of this reinforced section, where it is demonstrated that higher stresses are present, is being observed closely. More information on these stresses is provided below.

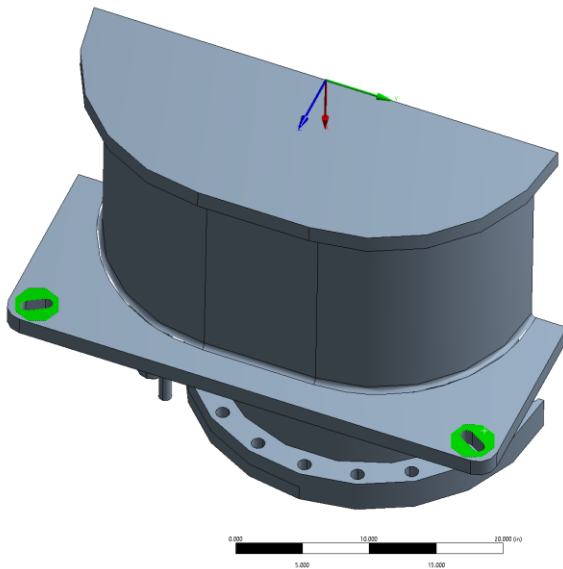


Figure C.5. Tank vertical supports boundary conditions.

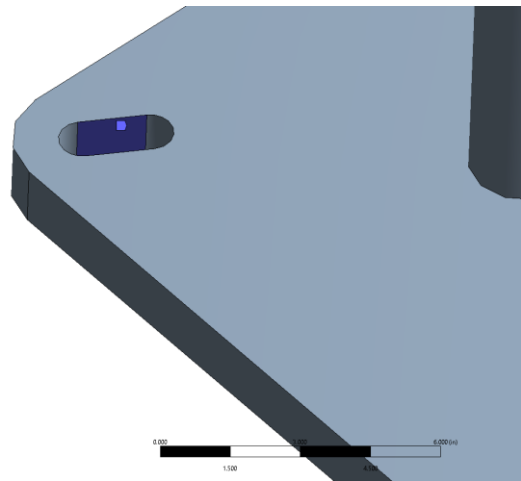


Figure C.6. Tank lateral boundary condition.

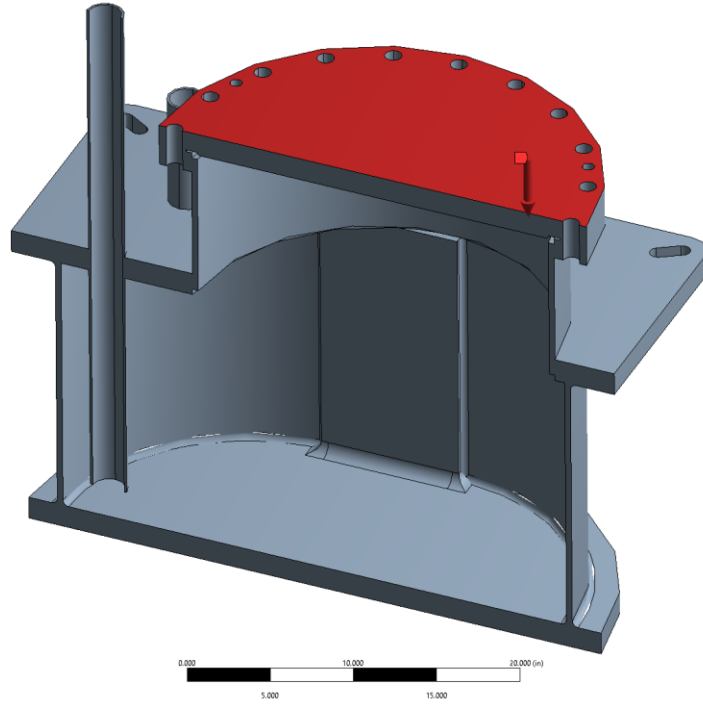


Figure C.7. Pump assembly load of 1,000 lbf.

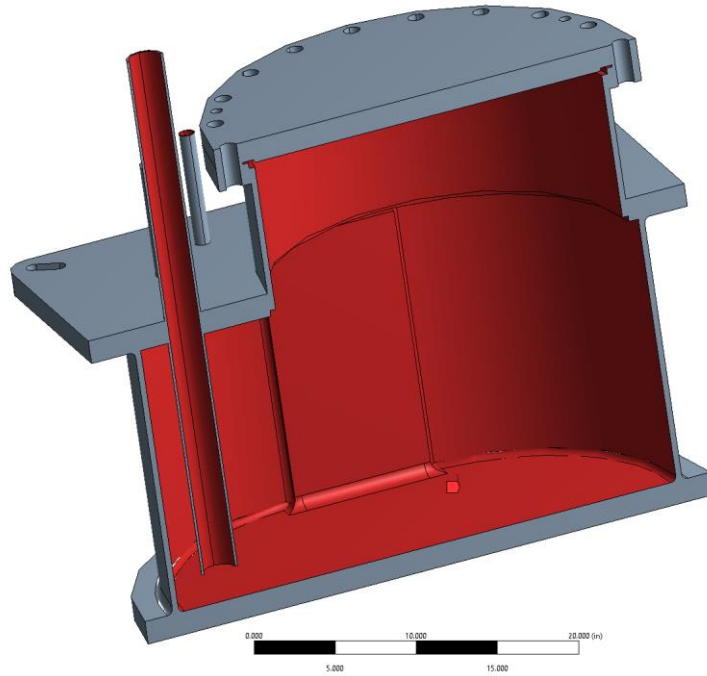


Figure C.8. Pressure of 21.5 psi applied to surfaces shown in red.

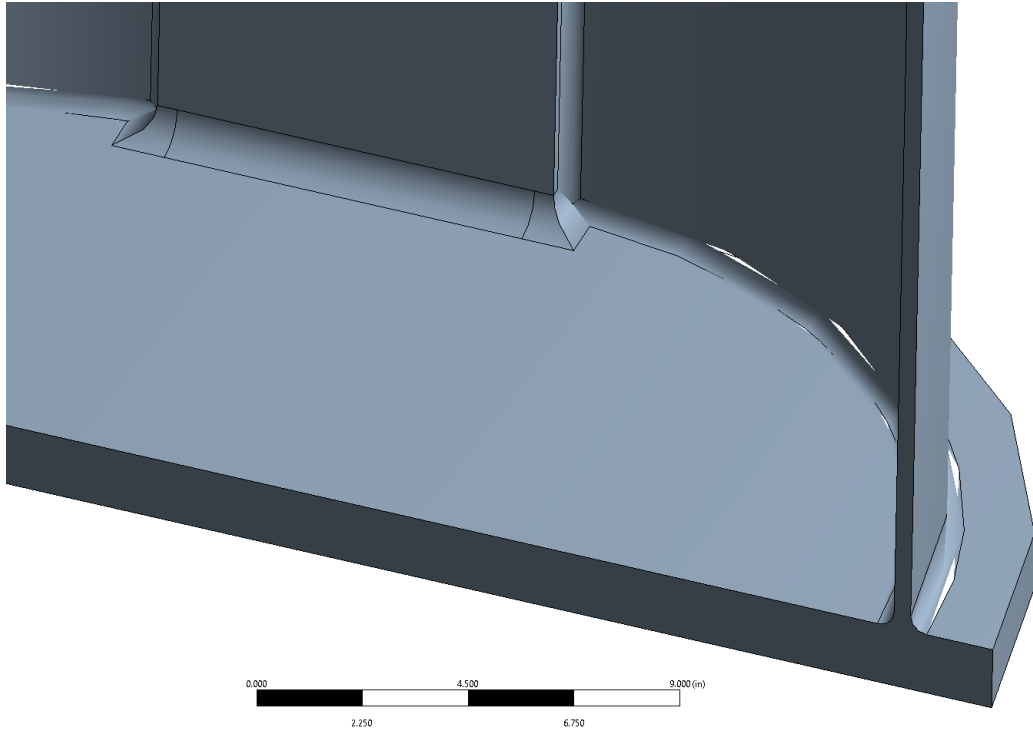


Figure C.9. Section reinforced with fillet welds.

C.4 MATERIAL PROPERTIES

The tank is fabricated from alloy C-276, a nickel-molybdenum-chromium superalloy. Applicable temperature-dependent material properties used for the simulation were taken from the Haynes International and Special Metals material specifications. The properties are provided in Table C.1 and Table C.2. The modulus of elasticity values at 600 and 700°C were not provided in the specifications and were therefore calculated using extrapolation.

Table C.1. Temperature-dependent mean coefficient of thermal expansion

Temperature (°C)	Mean coefficient of thermal expansion (μm/m°C)
100	12.2
200	12.4
300	12.9
400	13.2
500	13.5
600	13.6
700	14.1
800	14.8

Table C.2. Temperature-dependent modulus of elasticity

Temperature (°C)	Modulus of elasticity (GPa)
RT	205
200	195
300	189
400	183
500	178
*600	172
*700	166

*Extrapolated values

C.5 FEA RESULTS FOR 21.5 PSI TANK PRESSURE

The resulting von Mises stresses of the inside and outside of the tank are shown in Figure C.10 and Figure C.11. The peak stress in the model exists exclusively on the corner edge of the inside weld of the reinforced section, as shown in Figure C.12, for tank pressures above a couple psi. The stress along the bulk of the weld was also probed in the area indicated in Figure C.13.

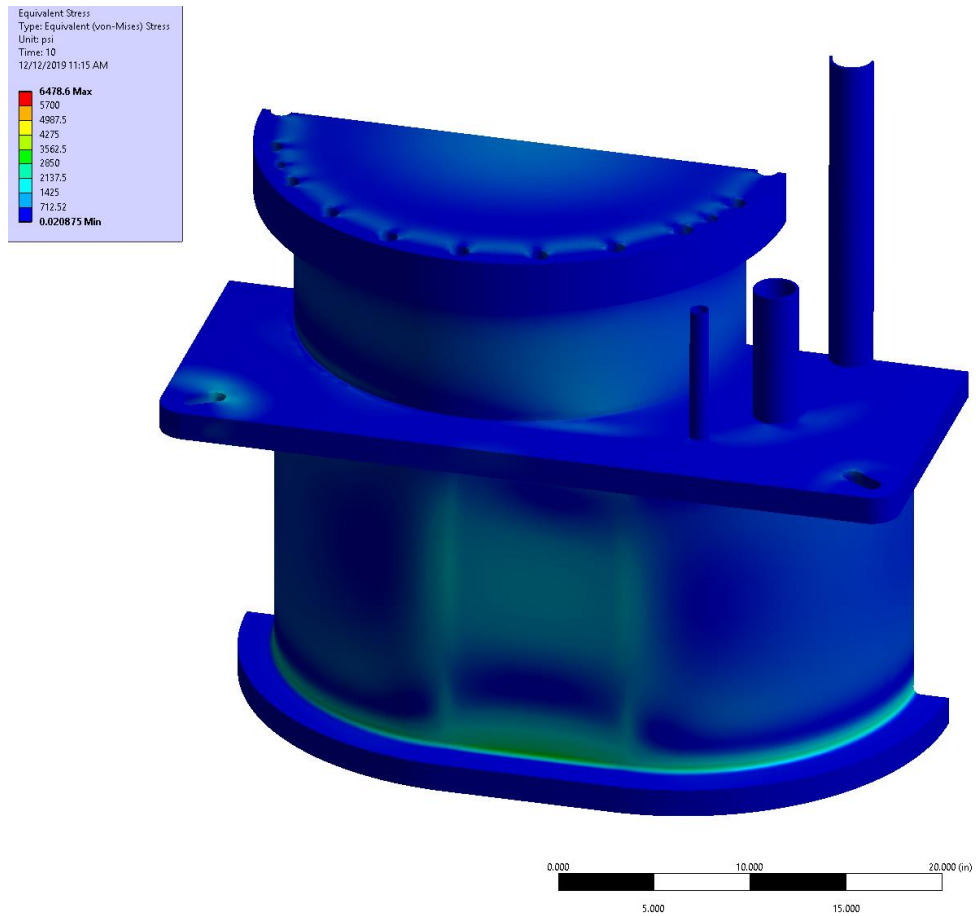


Figure C.10. Tank external von Mises stress results for tank pressure of 21.5 psig.

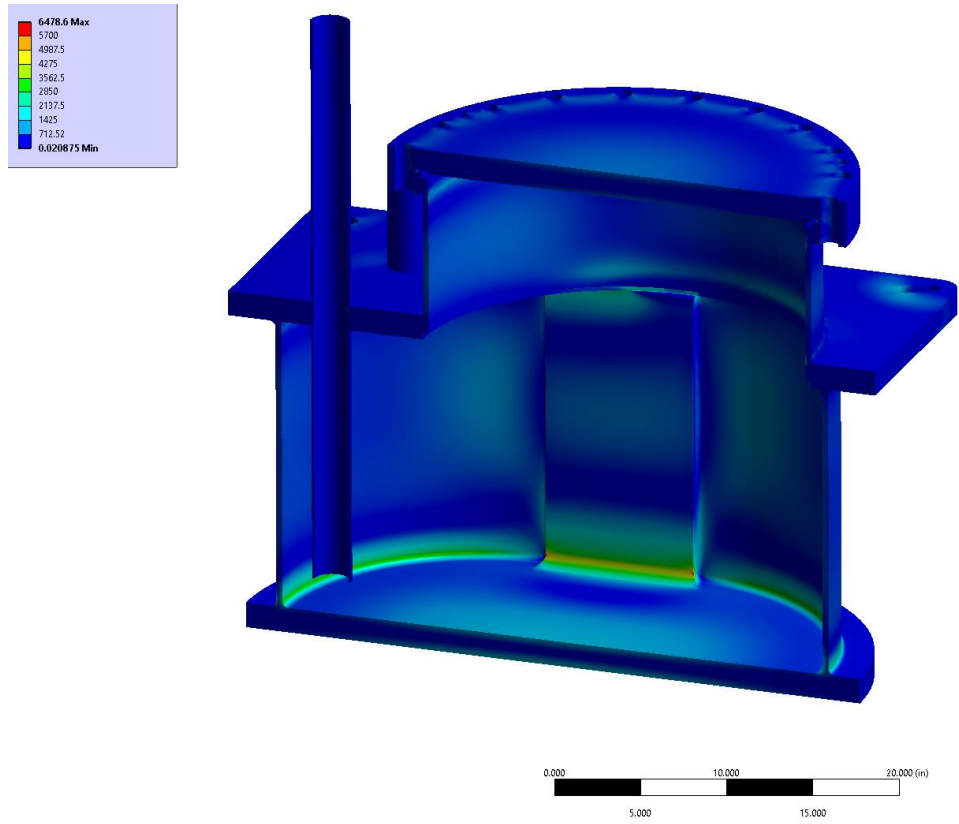


Figure C.11. Tank internal von Mises stress results for tank pressure of 21.5 psig.

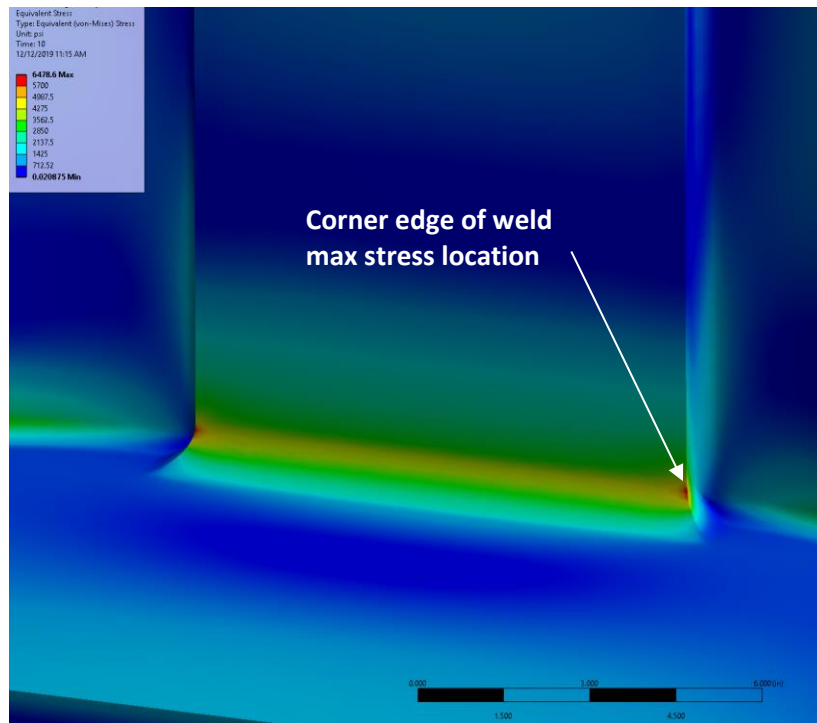


Figure C.12. Detail of von Mises stress results for tank pressure of 21.5 psig: reinforced section.

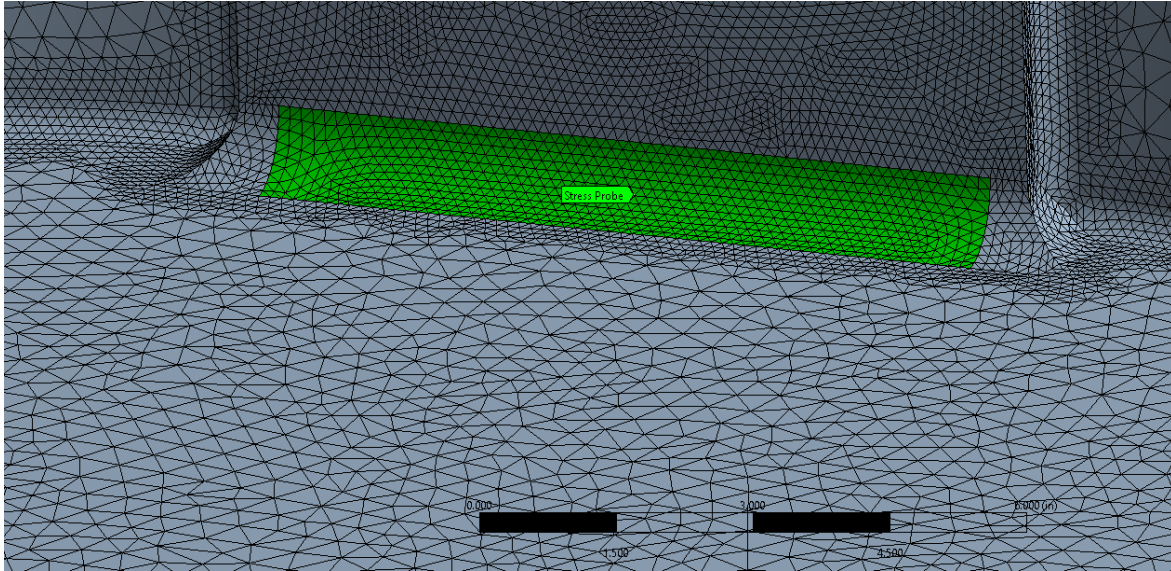


Figure C.13. Inside bottom edge von Mises stress results.

C.6 FEA RESULTS FOR PARAMETRIC VARIATION OF TANK PRESSURE

The model was solved for variations in the tank pressure from 0 to 30 psig. Figure C.14 charts the maximum stress (typically located at the corner edge of the weld) and the peak stress in the region noted in Figure C.13 vs. the applied internal tank pressure. At a tank pressure of 21.77 psig, the FEA indicates a maximum stress of 6.56 ksi which is located at the corner edge of the weld (location illustrated in Figure C.12).

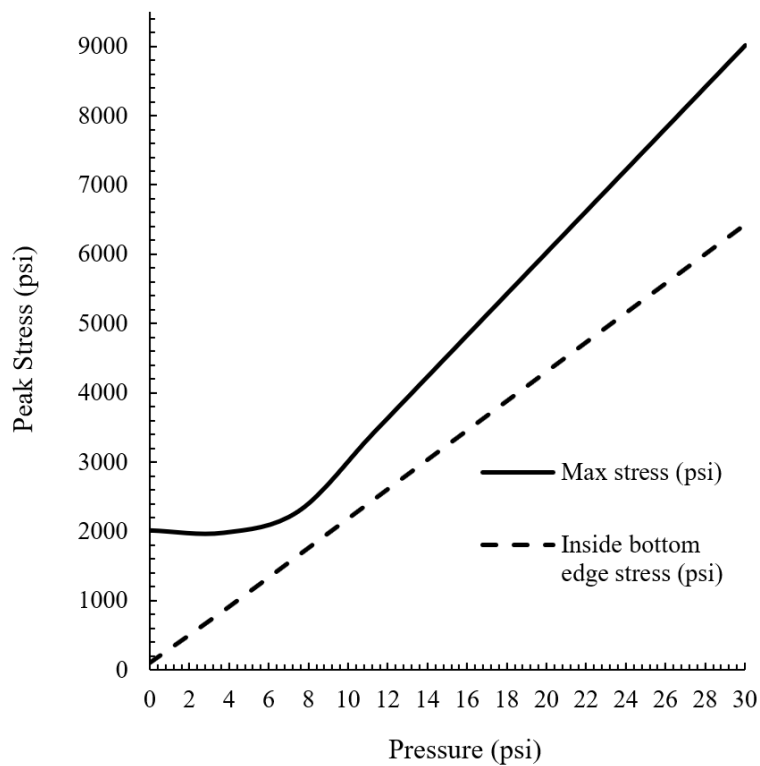


Figure C.14. Tank pressure vs. maximum stress in the pump tank assembly.

C.7 TANK PRESSURE RELIEF SETPOINT

As noted in Section 2.3, alloy C-276 is code rated up to 676°C in the ASME 2010 BPVC. For greater temperatures, allowed stresses were determined using the ASME analysis methodology and data from a major material manufacturer. At elevated temperatures of interest, the allowed stress is limited by its long-term creep behavior. For 1,300°F (705°C), the analysis of the manufacturer creep data yielded a recommended allowed stress of 6.56 ksi.

Based on the FEA and using an allowed stress of 6.56 ksi, the proposed pressure relief setpoint is 21.5 psig for a vessel temperature limit of 1,300°F (705°C).

Other supporting considerations:

- The vessel will be limited to ≤ 3 years of cumulative service at elevated temperature.
- Because the vessel is on the cold side of the loop, it will generally be operated at $< 700^\circ\text{C}$.
- At least 8 thermocouples will monitor the vessel temperature. An automated control system will control the tank temperature and will include predefined heater trips to prevent over-temperature.
- As illustrated in Figure C.10, Figure C.11, and Figure C.14., the stresses in most of the vessel are significantly lower than the stress at the corner edge of the weld shown in Figure C.12.
- Material test coupons will be incorporated into the loop for periodic testing.
- The vessel is surrounded by a 4-inch-high temperature insulation jacket with inner and outer fiberglass fabric sheets. Additional personnel barriers can be incorporated per environmental, health, and safety personnel guidance.

